POLITECNICO DI MILANO

Dipartimento di Fisica

Attosecond Transient Reflection for the Study of Electron Dynamics in Solids

Supervisor:

Dr. Matteo Lucchini

Tutor:

Prof. Mauro Nisoli

PhD thesis by:

Giacinto Davide Lucarelli

PhD cycle XXII

Contents

List of Figures

Introduction

The first study of ultrafast dynamical processes in matter is traditionally set in 1981, when Ahmed Zewail and coworkers first published a paper about quantum beats and dephasing in anthracene molecules with a picosecond temporal resolution [2]. The appearance of sub-picosecond lasers and of pulse compression techniques that allowed to obtain pulses with a duration of few femtoseconds [3], paved then the way to the development of ultrafast spectroscopy and femtochemistry. This research field is nowadays widely explored and has given astonishing results in the understanding of dynamical processes of physical, chemical and even biological interest [4].

Femtosecond temporal scales are intrinsically related to nuclear motion. The breaking of a chemical bond, vibrational oscillations in molecules, chemical reactions, structural motion in solids [5] are all processes that can be tracked with a femtosecond experiment. All the phenomena that are related to electron motion, however, occur on a faster time scale (from few femtoseconds to attoseconds), therefore pulses as short as few hundreds of attoseconds are required to study them.

The most widely employed technique for the generation of sub-femtosecond pulses takes advantage of the process of High-order Harmonic Generation (HHG) [6, 7, 8, 9]. The first train of attosecond pulses generated by means of HHG was measured by Paul and coworkers in 2001 [10]. In the same year, also the first generation of isolated attosecond pulses was demonstrated [11]. The possibility to generate such short pulses gave birth to a new field of study of ultrafast processes: attosecond science. In the following years, various novel experimental and theoretical approach led to the investigation and the discover of many physical processes in atoms, molecules and, lately, condensed matter. In particular, there is a plethora of solid-state physics processes, which unfold on a time scale that goes from few femtoseconds to attoseconds, such as ultrafast charge injection, dynamical Franz-Keldysh effect [12], electron photoemission delays and core-hole dynamical screening [13, 14]. Some experimental technique were implemented for their study. Among them, one of the most succesfully used in the last decade is called Attosecond Transient Absorption Spectroscopy (ATAS). ATAS is a full optical two-colour pump-probe technique. A pump pulse, usually in the near-infrared (NIR) range, induces a modification in the physical properties of the sample. These modifications are temporally resolved by detecting the variations in the trasmittance of a probe pulse, tipically the attosecond extreme ultraviolet (XUV) pulse, as a function of the pump-probe delay. ATAS has been successfully applied in a number of interesting studies (e.g. in [15, 16, 17, 18]), but has an intrinsic experimental limitation: since transmitted XUV light has to be detected, the thickness

of the sample must be very small (tens to hundreds of nanometers). It is very hard to realize such thin single-crystal samples and this substantially limits the applicability of ATAS. Moreover, heat transfer in thin solids is very inefficient leading to unwanted persistent contributions in the absorption spectrum such as heat-induced band shifts [19].

To overcome these limitations, one can change the geometry of the experiment, looking at the XUV radiation reflected by the sample rather than the transmitted one, thus performing an Attosecond Transient Reflection Spectroscopy experiment. Up now, there is only one article published on a peer reviewed journal reporting a transient reflection experiment in the XUV spectral range about femtosecond tracking of carrier relaxation in Germanium by the group of professor S. Leone [20].

I carried out my PhD work in the high energy attosecond laboratories of the Department of Physics of Politecnico di Milano. I dedicated the first part of my research activity to build and characterize a novel beamline for the realization of experiments on bulk solid targets with sub-femtosecond temporal resolution in a transient reflection spectroscopy scheme. In the second part of my PhD research, I applied this setup to the study of the ultrafast dynamics around a semi-core exciton in crystalline bulk MgF_2.

This thesis is organized as follows:

- In the first chapter I will summarize some of the most important experimental techniques employed in the field of attosecond physics and give some examples of their application. In particular I will outline briefly the most important results achieved by attosecond physics in the study of ultrafast dynamics in condensed matter.

- In the second chapter, I will describe the experimental setup for the realization of attosecond transient reflection spectroscopy experiments, that we built from scratch. In this section, I will also point out the main issues we had to face during the build-up stage and describe some setup characterization experiments.

- In the third chapter, the results of the very first attosecond transient reflection spectroscopy experiment will be presented. Ultrafast dynamics around a semi-core exciton in MgF_2 have been studied.

- The fourth and last chapter reports a summary of the achievements of my PhD activity and an introduction to the possible future applications and improvements of the newly built beamline.

Chapter 1

Attosecond Science

Attosecond science gives very powerful tools for the study of electronic dynamics and fundamental physical processes in atomic, molecular and solid-state systems. Isolated pulses and train of attosecond pulses, are now routinely available in many laboratories and employed to perform various kinds of experiments [21].

One of the most usual way to perform experiments in the attosecond spectroscopic domain is exploiting the two color XUV-NIR/VIS pump-probe approach. The pump pulse initiates a process; the induced change in an observable are addressed measuring its effect with a probe pulse after a certain delay. If the physical process is repeatable, the full dynamics of the system can be observed by precisely scanning the delay between the two pulses.

In the last few years, attosecond science has allowed us to address many processes in the field of atomic, molecular and condensed-

matter physics and impressive advances have been obtained from both the experimental and theoretical points of view. In this first chapter the main experimental techniques employed in attosecond science are outlined and important results are discussed.

1.1 Time Resolved Photoemission Spectroscopy

The possibility to have a robust way to generate attosecond extreme-ultraviolet (XUV) pulses (by means of HHG process [6, 7, 8, 9]) enabled access to electron dynamics on their natural time scales. In particular photoionization and photoemission dynamics have been investigated in various systems, ranging from atoms ([22, 23, 24]) and molecules (review in Ref. [25]) to condensed matter systems such as solid surfaces ([13, 26, 27, 28]) and nanoparticles ([29]).

The most widely used techniques for the study photoemission dynamics are the Reconstruction of Attosecond Beating By Interference of Two-photon Transitions (RABBITT, [30]), attosecond streaking spectroscopy and Time Resolved - Angle Resolved Photoemission Spectroscopy (TR-ARPES). In the two following sections, I will focus on the description of the first two techniques since they were employed also during my PhD work, as I will report in chapter 3.

1.1.1 RABBITT

One way to investigate time delays in photoionization is to employ the RABBITT technique [31]. It consists in the acquisition of photoemitted electron spectra from a noble gas as a function of the delay between the attosecond pulse train (APT), which ionizes the gas, and a dressing NIR pulse. Since in the HHG scheme only odd harmonics are generated, the energy of the photoemitted electrons is an odd multiple of the NIR energy minus the ionization potential of the target gas [32]. It can be written in the form:

$$E_e = (2q+1)\hbar\omega_{NIR} - I_p, \tag{1.1}$$

where ω_{NIR} is the NIR angular frequency and q is an integer number. After the photoemission, electrons can interact with one or more NIR photons that induce additional transitions in the continuum. In particular, if we only consider interactions with a single NIR photon, it can be either absorbed or emitted. Therefore, electrons with an energy corresponding to an even multiple of the NIR photon energy are recorded, thus generating the so-called sidebands as it is represented in Figure 1.1.

In case of low NIR field intensity, we can describe this using a second-order perturbation theory. In this case, each harmonic has only one sideband per side. Thus, the signal of each sideband is given by the contribution of just two neighboring harmonics, via two different quantum paths which may interfere. As a result, the sideband oscillates as the delay τ between the IR and XUV pulses is scanned. Applying Fermi's golden rule in the second-

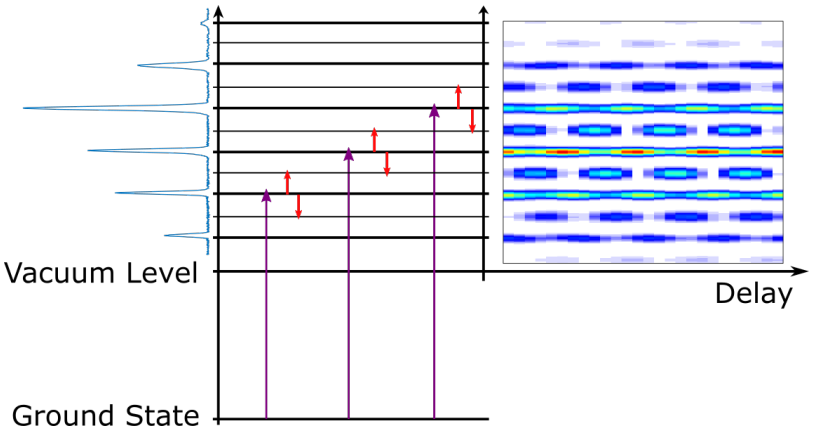

Figure 1.1: Schematic representation of the origin of a RABBITT trace. XUV photons are absorbed (purple arrows) and electrons are emitted from a gas atom. The photoelectrons energy spectrum, then presents discrete peaks, which correspond to transitions induced by single-photon absorption of XUV harmonics, separated by $2\hbar\omega$, where ω is the frequency of the driving IR pulse. When there is temporal overlapping between XUV and IR pulses, the photoelectrons interact with one IR photon which is either absorbed or emitted (red arrows), giving origin to additional peaks in the photoelectron spectra at $\pm\hbar\omega$ with respect to the peaks generated by the XUV harmonics. This, populates the so-called sidebands (SB), while depleting the harmonics (HH). Upon changing the delay between XUV and IR pulses, the sideband amplitude oscillates at twice the frequency of the IR field.

order perturbation framework and assuming monochromatic NIR field and XUV harmonics, the sideband intensity can be written as:

$$I_{2q}(\tau) \propto 1 + \cos(2\omega_{NIR}\tau - \Phi_{SB}), \tag{1.2}$$

where

$$\Phi_{SB} = \Delta\theta_{HH} + \Delta\theta_{Atom} - \theta_{NIR} \tag{1.3}$$

being θ_{NIR} the NIR phase, $\Delta\theta_{HH}$ the phase difference of two adjacent harmonics, related to the chirp of the XUV pulses and $\Delta\theta_{Atom}$ a term related to the atomic photo-ionization process. This last term is mainly due to two independent contributions: a scattering term called the Wigner delay [33], related to the delay introduced by the propagation of the electron wavefunction in the parent ion potential rather then in free space, and the continuum-continuum contribution, due to the absorption or emission of the IR photon.

With this technique, one can thus extract information on the XUV attosecond pulse train chirp, maily considering $\Delta\theta_{HH}$ (given that $\Delta\theta_{Atom}$ is much smaller) or about the time delay in photoemission, focusing on $\Delta\theta_{Atom}$ (since $\Delta\theta_{HH}$ is independent from the target). As an example, RABBITT approach was used by Klunder *et al.* to investigate photoionization from 3p and 3s shells of argon gas [23]. In this experiment they were able to observe that electron wavepackets coming from 3p shells is delayed with respect to the ones coming from 3s shells by few

tens of attoseconds. The first RABBITT experiment on a solid state sample was performed by Locher *et al.* in 2015 [34]. From that measurements, it was possible to show that neither electron transport nor initial state localization alone can be used to fully explain the measured photoemission delay in solids, and so that a key role is played by final state effects.

1.1.2 Attosecond streaking

Another technique, that is technically analog to RABBITT, is the attosecond streaking technique [35]. In this case, a target is photoionized by a single XUV attosecond pulse in presence of an intense and low frequency electromagnetic field (as the one associated to the NIR pulse used for the HHG itself). To describe the process, let's consider a target with a ionization potential I_p, ionized by a XUV field $\mathbf{E}_X(t)$ in the presence of an IR field $\mathbf{E}_{IR}(t) = \partial\mathbf{A}/\partial t$, described by the vector potential $\mathbf{A}(t)$ and shifted by a variable delay τ (atomic units are used). The transition amplitude to the final state in the continuum $|\mathbf{v}\rangle$ of the extracted electron with momentum $\mathbf{v}$, can be described, in the strong field approximation (considering the final state to be a plane wave), by the formula [36] (atomic units are employed):

$$a(\mathbf{v},\tau) = -i\int_{-\infty}^{+\infty} e^{i\phi t}\mathbf{d}_{\mathbf{p}(t)}\cdot\mathbf{E}_X(t-\tau)e^{i(W+I_p)t}dt, \tag{1.4}$$

$$\phi(t) = -\int_{t}^{+\infty} dt'[\mathbf{v}\cdot\mathbf{A}(t') + \mathbf{A}^2(t')/2]. \tag{1.5}$$

Here $\mathbf{p}(t) = \mathbf{v} + \mathbf{A}(t)$ is the instantaneous momentum of the free electron in the laser field, $\mathbf{d_p}$ is the transition dipole matrix element from the initial state to the final continuum of states and $W = \mathbf{v}^2/2$ is the electron final kinetic energy. In equation 1.4, the scalar product $\mathbf{d}_{\mathbf{p}(t)} \cdot \mathbf{E}_X$ represents the electron wavepacket generated in the continuum by the XUV field, on which it is induced a temporal phase modulation $\phi(t)$ (given by the Equation 1.5) by the dressing NIR field. We can qualitatively describe this effect as follows: the trajectory that the photoelectron follows, from the parent ion to the detector, depends on the time at which it is photoemitted by the XUV within the NIR optical cycle, since it depends on the strength of the dressing field with which it interacts. As a consequence, the phase that the wavepacket accumulates in each trajectory is temporally modulated by the NIR field. It is worth noting that, because of the scalar product $\mathbf{v} \cdot \mathbf{A}$, the photoelectrons need to be observed in a precise direction for the phase modulation to be effective. The 2D trace obtained by acquiring photoelectron spectra at different XUV-NIR attosecond delays is the so-called streaking trace (a typical one is shown in Figure 1.2).

This technique allows one to gather information both about the characteristics of the pulses that are used to acquire the trace and about the ionized material.

Indeed, one of the most widely applied technique for the reconstruction of isolated attosecond pulses, called FROG-CRAB (Frequency Resolved Optical Gating for the Complete Reconstruction of Attosecond Bursts) [36] relies on the acquisition of a streaking trace and on the employment of an iterative algorithm

to get the full reconstruction of the XUV attosecond pulses and the NIR few-femtosecond pulses which generate the trace. In fact, the value $|a(\mathbf{v},\tau)|^2$, representing the electron photoemission probability as a function of its momentum and the delay, is almost formally identical to a FROG spectrogram [37], where the temporal gate is the phase $e^{-\phi(t)}$ defined in Equation 1.5. In order to have a complete formal equivalence, neither the pulse nor the gate should be a function of the final electron momentum. This issue can be solved with the application of the Central Momentum Approximation (CMA), thus approximating $\mathbf{v}$ to the central value of the momentum in the photoelectron spectrum generated by XUV photoionization. This approximation holds if the initial momentum of the photoelectrons $\mathbf{v}$ after the photoionization process is much larger than the maximum momentum boost $\Delta\mathbf{v}_{max}$ induced by the NIR field. Several iterative algorithms are then available for the reconstruction of the NIR and XUV field starting from the streaking trace, such as PCGPA [38] (the most widely used), LSGPA [39], VTGPA [40] and ePIE [41].

Attosecond streaking has also been used for the investigation of electronic properties of materials. It was employed, for example, to measure the relative photoemission delay due to electronic correlation effects in helium [42]. Electron photoemission, indeed, is usually treated as a one-particle phenomenon, taking advantage of the so-called single-active electron approximation. With attosecond streaking spectroscopy, it was possible to observe the failure of this approximation by recording up to 6 as delay of the dislodged photoelectron due to electronic correlations. It was measured the photon-energy-dependent emission timing of elec-

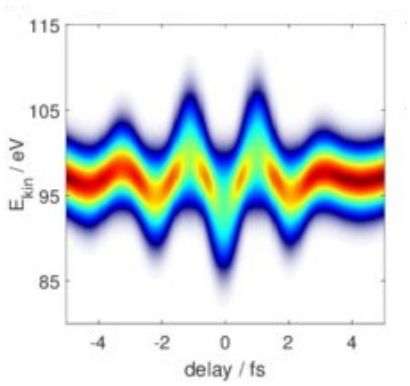

Figure 1.2: Example of attosecond streaking trace simulated in helium with a 350-as XUV pulse (spectrum centered at 110 eV) and a 6-fs transform limit NIR pulse.

trons, released from helium by an XUV photon, either leaving the ion in its ground state or exciting it into a shake-up state (see Figure 1.3).

More recently, attosecond streaking has been applied also on solid state samples. The first application of this technique on condensed matter was performed by Cavalieri and co-workers in 2007 [43]. In that work, they demonstrated the possibility to have direct time-domain access to electron dynamics with attosecond resolution by probing photoemission from single-crystal tungsten. With their experiment, they showed a photoemission delay of approximately 100 attoseconds between photoelectrons coming from localized core states of the metal, and those that originate from delocalized conduction-band states (see Figure 1.4).

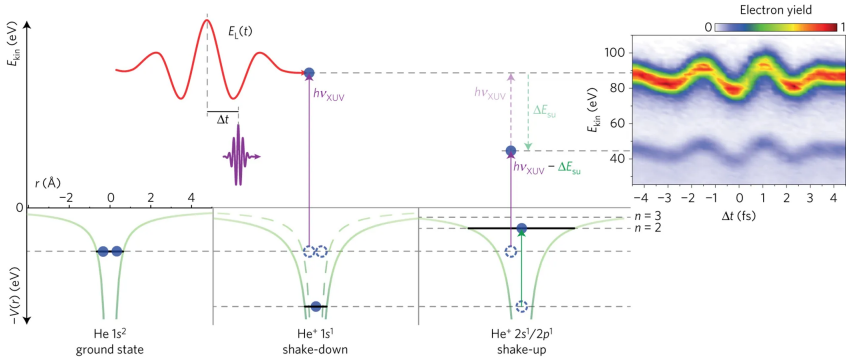

Figure 1.3: Electron photoemission from helium ground state (left panel) with a ionization potential of 24.6 eV products the release of the electron with a kinetic energy equal to the difference between XUV photon energy and ionization potential into the continuum (middle panel). Ionic potential rearranges after the electron loss because of the modified screening of the nucleus, and the remaining electron occupies a more tightly bound state (so-called shake-down process or direct photoemission). Alternatively, with lower probability, electron emission may take place along with the excitation of the leftover electron into one out of a series of shake-up states n (right panel). Due to electronic correlation, the emitted electron kinetic energy is lowered by the shake up state excitation energy ΔE_{su}. In the presence of a dressing laser field, the kinetic energy distribution of both quantum pathways is modulated as described in Section 1.1.2, allowing for an accurate determination and comparison of the electron release times. Reproduced with permission from [42]

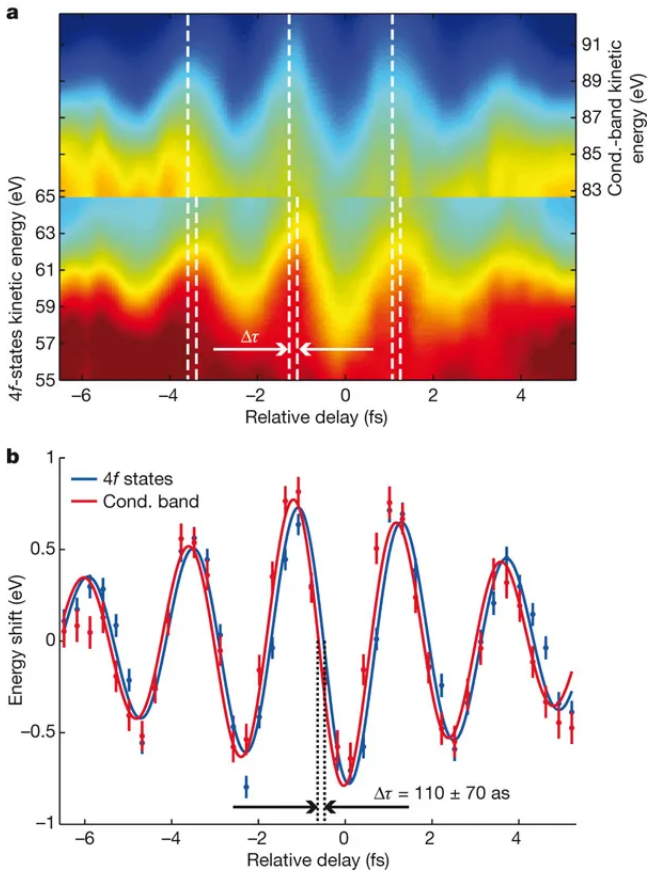

Figure 1.4: **a**. Streaking traces of electrons coming from bound 4f states and conduction-band of tungsten metal sample, after cubic-spline interpolation of the measured data (but no background subtraction). The region between 65 eV and 83 eV is omitted for easier comparison of the edges of the 4f and conduction-band peaks. The evident small shift in the relative delay is indicated by the white dashed lines through the fringes. **b**. Comparison between the extracted Center of Mass (COM) of the two photoelectron traces. The energy intervals for the calculations of the COMs are: 47–66 eV for the 4f photoemission and 66–110 eV for the conduction-band photoemission. Reproduced with permission from [43]

.

1.2 Attosecond Transient Absorption Spectroscopy

In this section, I will focus on a different kind of spectroscopic technique, called Attosecond Transient Absorption Spectroscopy (ATAS). Transient absorption is an all-optical technique and does not depend on the photoemission of electrons. Thus, time and frequency resolution are not interdependent through the uncertainty principle, and can be optimally short and narrow, respectively. This advantage of transient absorption was discussed by Pollard et al. [44] in the context of visible pulses, but directly translates to the XUV attosecond domain. Transient absorption is a well-established technique in frequency regions spanning ultraviolet, visible and mid-infrared. A pump pulse first generates a population in one or more excited states of the system. The population is, then, allowed to evolve freely for a defined amount of time, after that, a probe pulse induces transitions to other excited states. By spectrally-resolving the absorption of the probe pulse, signatures of the present state of the system can be recognized. In practice, the probe spectrum is measured at each pump-probe delay step, with (I_{on}) and without (I_{off}) the presence of the pump pulse, and the observed quantity is the change in absorption or in optical density of the sample, $\Delta OD = -log_{10}(I_{on}/I_{off})$.

1.2.1 ATAS in Gas Phase Samples

The complications of Transient Absorption in the IR to ultraviolet frequency range occur when spectral features from different

excited states overlap, either because of small shifts or broadband transitions. This may prevent a simple assignment of the observed features to chemically relevant information. This obstacle can be overwhelmed by using much shorter wavelengths. The core levels of most elements have very distant ionization energies. As known from synchrotron measurements, the so-called core absorption edges are located indeed in the XUV and X-ray regions, and their spectrum is very sensitive to the electronic environment. Thus, performing transient absorption with an XUV probe gives more information than in the visible, for example on the oxidation state, coordination or bond nature [45, 46]. Moreover, clearly, the possibility to have Single Attosecond Pulses as probe, phase locked with the pump field (the HHG driving field), gives unparalleled temporal resolution to the experiments.

ATAS has been successfully applied in numerous experiments on gas phase targets. As an example, Goulielmakis and co-workers [47] in 2010 were able to observe the time evolution of the electronic wavepaket formed by a superposition of states in ionized krypton atoms generated by a a few-cycle visible pulse. Probing with XUV Isolated Attosecond Pulses (IAPs) centred around the $4p \rightarrow 3d$ core-to-valence transition of the cation, they observed strong oscillations in the absorption features at a frequency of 6.3 fs due to the wavepacket created between the two spin-orbit splitted states of the krypton cation (split by 0.67 eV). By extracting the amplitude and phase of this oscillation, the authors were able to reconstruct the time evolution of the electronic wavepacket with sub-femtosecond temporal resolution (see Figure 1.5).

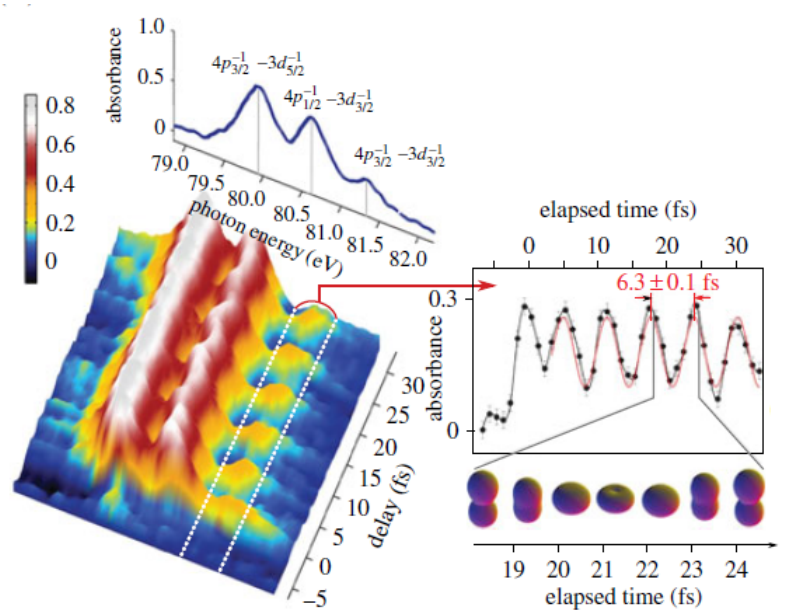

Figure 1.5: The time evolution of the ATAS spectrum in krypton gas is shown with the corresponding transitions. From the oscillations in the time trace,it is possible to reconstruct the wavepacket temporal evolution. Adapted with permission from [47]

Attosecond Pulse Trains (APTs) have been employed, instead, in another pioneering work, which employed ATAS technique for the study of ultrafast dynamics in noble gasses. Holler *et al.* [48] in 2011, managed to resolve rapid oscillations in the absorption spectrum of the individual harmonics around the helium ionization threshold as a function of time delay with respect to a superimposed, moderately strong NIR laser field. The phase difference between the absorption modulation of each harmonic

was measured and its origin was attributed to the interference of transiently bound electronic wave packets.

1.2.2 ATAS in Condensed Matter

The capability of ATAS, broadband probing, element-specificity and atto to femtosecond temporal resolution, can be profitably used also in the study of condensed matter systems.
The behavior of an electron in periodic lattice potentials has been a fundamental problem of solid-state physics, starting from the early works of Drude [49], Sommerfeld and Bethe [50] and Bloch [51], until today. In practice, this has been investigated by observing the response of the system to a stimulation, such as heat or electromagnetic radiation. The induced alteration of the system is then explained through a response function such as the heat capacity or the dielectric function. Over the years, many kind of probes identified the various processes controlling electronic dynamics, as electronic correlations, magnetic effects, or lattice vibrations [52]. Along with this knowledge came the potentiality of driving these dynamics not just far away from their equilibrium, but with excitation strong enough to redefine the system eigenstates. Intense electric fields can now be used to strongly modify the band structure of the material enough to change its properties. Zener tunnelling [53, 54], Wannier–Stark localization [55, 56] and the Franz–Keldysh effect [12] are some examples. Short XUV to X-ray pulses, which allow to access both the electronic and the structural effects, are a unique probe of condensed matter properties. When a solid is illuminated by

a light pulse, the medium complex refractive index is transiently modified. The cause of this change is the motion of the medium constituent electrons as well as the movement of the lattice. As mentioned in the previous section for gas phase, electrons can react on attosecond time scales, therefore ATAS is one of the best tools to fully track their dynamics.

Many important results have been obtained applying ATAS on different solid samples. It is worth to mention, in particular, some experiments performed to study, with a sub-cycle resolution, the processes driven by an intense few-femtosecond pulses. The first of these experiments was performed by Schultze et al. [57] in silicon dioxide (SiO_2), a 9 eV direct bandgap dielectric material. A 125 nm thick SiO_2 sample (attenuation length for SiO_2 at 105 eV $\sim$ 82 nm) was pumped by a visible-near infrared (VIS–NIR) pulse of less than 4 fs duration, and probed by a 72 as IAP. The attosecond pulse energy was selected in order to match the Si 2p states (the L2,3-edge, laying around 99 eV), and make transitions from core-levels to the Valence Band (VB) and Conduction Band (CB) possible. The VIS-NIR pulse (1.5 eV central energy) is not able to promote carriers from the valence to the conduction band. As a consequence, the absorption does not change when the pump and probe pulses do not overlap in time. On the other hand, the XUV absorption varies significantly during the pump-probe overlap (Figure 1.6e). In this delay region, the absorption amplitude oscillates at twice the pump laser frequency, thus suggesting that the involved mechanism is strictly connected to the driving electric field squared. This has been interpreted as a disclosure of Wannier–Stark localization [55]. In this phenomenon, a strong

electric field generates highly localized electronic states at lattice sites. At the same time, the bands of the material bend as the field strength increases. If the field is strong enough, the shifted bands of neighboring lattice sites may cross, thus generating a mixing of valence and conduction bands. If we project it back to the field-free band structure, this resembles a transient electron (hole) population in the CB (VB). Schultze *et al.* [57] showed that this effect is fully reversible, thus giving a way towards the control of the material dielectric function at twice the optical frequency, which means almost at the petaHertz level. This represents a significant progress if compared to actual electronics, which operate, at most, at teraHertz frequency. From this result, we can anticipate that the ratio between the bandgap energy, the driving photon energy and the pump intensity, i.e. the excitation regime, is fundamental to define the physics at play. Therefore, it is worth to introduce the definition of the *Keldysh parameter* γ [58]:

$$\gamma = \frac{\omega}{eE_0}\sqrt{m^*\Delta_g}, \tag{1.6}$$

where e is the electron charge, E_0 and ω are respectively the driving field amplitude and angular frequency, m^* is the reduced mass of the electron hole pair and Δ_g is the material band gap. For $\gamma > 1$, the dominant physical mechanism is expected to be multiphoton excitation. If $\gamma < 1$, then tunneling is expected to be prevailing. The latter is the regime that was employed in the ATAS experiment on pure silicon (direct band gap $\sim$ 3.2 eV) performed again by Schultze and co-workers [59]. Here, electrons

are injected into the conduction band by a strong IR field. It was interesting to notice that, since the VIS-NIR photon energy (1.1 - 2.7 eV) is rather smaller than the bandgap, a nonlinear excitation mechanism for the carrier injection is implied. In particular, if one focuses on the ultrafast build-up of the electronic population, (shown in Figure 1.6b), one may notice a step-wise growth, synchronized with the oscillations of the electric field. This was explained by the fact that γ in this experiment was ~ 0.5, and then, at each extremum of the driving field, carriers are allowed to tunnel from the VB to the CB. The case of $\gamma > 1$, in which multiphoton excitation is expected to be dominant, has been studied by Mashiko *et al.* [16] in gallium nitride (GaN, $E_g = 3.35$ eV, Figure 1.6c). They employed a pump pulse intensity I about 100 times smaller than in the previously described experiment. Since the Keldysh adiabaticity parameter scales as $\gamma \sim I^{-1/2}$, the excitation is definitely into the multiphoton regime. Differently from the previous studies, where the XUV attosecond pulses probed core-to-valence transitions, in this case they were employed to probe transitions from the VB and/or CB to the continuum. As shown in Figure 1.6c, the absorption variation oscillates at three times the NIR field driving frequency, clearly evidencing the presence of three-photon absorption. Interestingly, this frequency corresponds to 1.16 PHz, therefore providing the very first direct observation of controlled optical driving above 1 petaHertz. A different regime (resonant excitation) was employed by Schlaepfer and co-workers in the study of a slightly lower bandgap material, gallium arsenide (GaAs) [18]. In this case, resonant one photon excitation from the VB to the CB is possible, which, intuitively,

may suggest a simple monotonic increase of the absorption induced by the pump. Schlaepfer and co-workers measured instead 2ω-oscillations across both the VB and CB (as shown in Figure 1.6a) by probing the system from the As 3d core level. They took advantage of theoretical simulations to separate the observed dynamic into inter- and intra-band contributions, showing that the laser-driven motion of electrons inside one band (intraband motion) can explain the findings. Moreover, this mechanism, surprisingly also increases the number of carriers injected into the CB by almost a factor of three. This opens a new perspective for resonant excitation in semiconductors. Ultimately, one may wonder what goes on in the intermediate situation, when real carriers excitation is possible, but the field is also strong enough to deform the band structure. Lucchini *et al.* [15] addressed this question by studying diamond, which has direct and indirect bandgaps of 7.3 and 5.4 eV, respectively. In this case, the NIR pump pulse is strong enough to inject real carriers in the CB by multiphoton absorption, making it very hard to disentangle this phenomenon from band-structure modifications. Therefore, the authors decided to use the XUV attosecond pulses to probe transitions from the lower VB to the higher CB, where carriers are not present. There, they measured strong oscillations at twice the NIR driving frequency (see Figure 1.6d), representative of a so-called dynamical Franz–Keldysh effect [12], in which the electronic wave functions are modified by the laser pulse, leading to oscillations in the XUV absorption coefficient. All of these results show the capability of ATAS of recording the electrons response during the interaction with a strong varying electric field with

sub-cycle time resolution.

1.3 Goal of the Project

The studies presented in the previous section give a physical insight into some of the most relevant questions in condensed matter physics and show the potential of ATAS to successfully address some of them. However, ATAS is a quite new field, currently still under development, and, at present, it is performed in a very small set of specialized laboratories around the world. This technique presents, however, some limitations in its applicability. The most significant one is that not all materials can be synthesized under the form of film thin enough to transmit XUV light, which means of the order of tens to hundreds of nm. Moreover, thin films conduct heat badly. So, it can often happen that the sample does not cool down between consecutive laser pulses. This may lead to unwanted persistent contributions in the absorption spectrum such as heat-induced band shifts [19]. Finally, ATAS is blind to the surface properties of the sample, preventing the possibility to study the chemistry of interfaces. A way to overcome these limitations is to change the geometry of the experiment and perform Attosecond Transient Reflection Spectroscopy (ATRS). This technique has rarely been implemented [20, 61] because it is more technically challenging, due to the reduction of an already exiguous XUV flux at the reflection interface and more difficult experimental implementation. Moreover, in ATRS it is not easy to place a gas target with a Time Of Flight (TOF) spectrome-

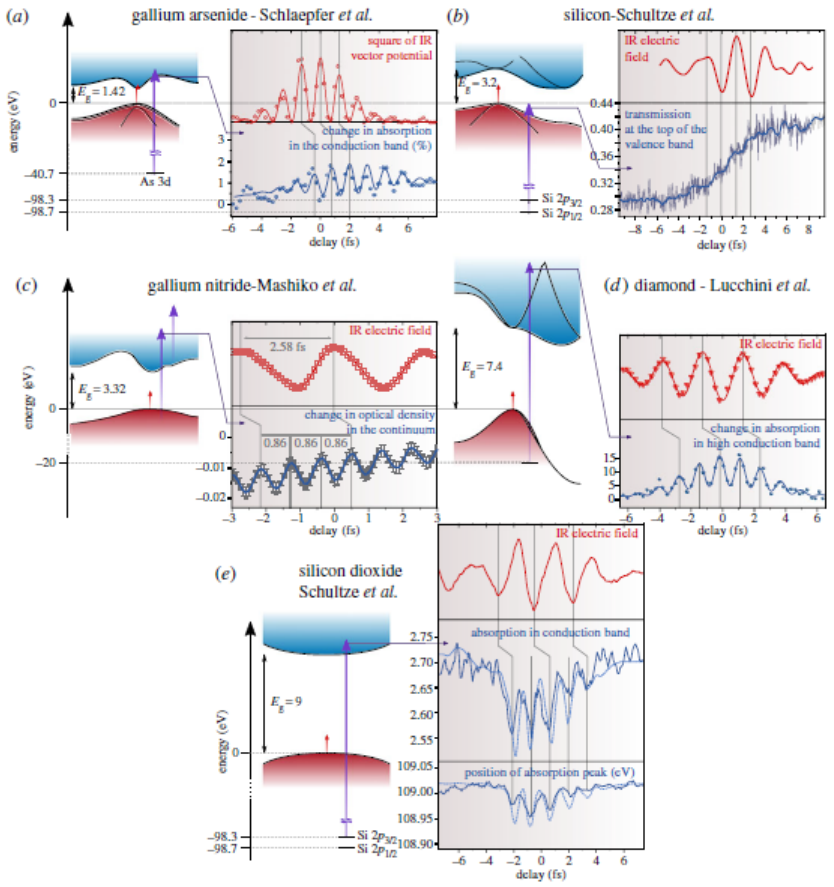

Figure 1.6: Summarizing picture of the five ATAS experiments presented in the text. The band structure of each material is sketched. The VIS-NIR pump pulse is represented with a red arrow and the XUV probe pulse is represented with a purple arrow. On the right, it is shown the VIS-NIR temporal profile measured by simultaneous streaking (red line), together with the transient absorption measurement (blue line). (a) Intra-band current in GaAs; (b) inter-band tunneling from the VB to the CB in Si; (c) multiphoton absorption in GaN; (d) dynamical Franz–Keldysh effect in diamond; (e) Wannier–Stark localization in SiO_2. Adapted from [60]

ter very close to the sample to acquire in situ a photoelectron streaking trace simultaneously with the ATRS trace in order to gather precise information on the field acting on the sample, as it is often done in transient absorption geometry. This restriction can however be overcome by adapting a technique already used in photoemission spectroscopy [62], which consists in focusing twice the beam in a sequential geometry, placing in the two foci, respectively, the noble gas target with the TOF spectrometer and the solid target under analysis.

Therefore, the goal of my PhD project was to set up from scratch and characterize a new two-foci beamline and employ it for the profitable execution of attosecond transient reflection spectroscopy experiments. In the next chapters of this thesis, I will describe the newly built setup and I will present and comment the very first ATRS experiment that has been performed using this setup on a magnesium fluoride sample.

Chapter 2

Experimental Setup

In this section, I will present the characteristics of the experimental setup. First, I will briefly describe the near infrared femtosecond laser system; then I will briefly present the hollow core fiber compression setup, used to further compress the time duration of the infrared pulses; eventually, I will illustrate the actual two-foci setup that we built during my PhD period for the realization of attosecond transient reflection spectroscopy measurements on solid samples, composed by an active stabilized interferometer, a first interaction region, where the reference experiment on noble gas takes place (first focus), a refocusing chamber, and a second interaction region, where the solid sample under study is placed (second focus).

2.1 Laser System

The laser system is a commercial AURORA 10 kHz by Amplitude Technologies. It is composed by a Ti:Sapph oscillator (Femtosource Rainbow), which seeds a three-stage chirped-pulse amplification (CPA) system pumped at 10 kHz by the high power frequency-doubled Nd:YAG Q-switched laser Etna HP by Thales (typical average power is 135 W). The system provides IR pulses (with a central wavelength of 800 nm) with an energy of 2 mJ and a FWHM temporal duration of 25 fs.

2.2 CEP Stabilization

The generation of Isolated Attosecond Pulses (IAP) by HHG has been experimentally demonstrated exploiting a number of experimental techniques [63, 64, 65, 66, 67]. All of them are based on the fundamental requirement that the driving laser field must be Carrier-Envelope Phase (CEP) stable. If we define the electric field of the generating pulses as the real part of:

$$E(t) = A(t)e^{i(\omega_0 t+\phi)} \tag{2.1}$$

(where $A(t)$ is the complex envelope of the electric field and ω_0 is the carrier frequency of the pulse), the so-called Carrier-Envelope phase term is ϕ and represents the temporal offset between the maximum of the envelope (assumed at $t = 0$) and the maximum of the electric field.

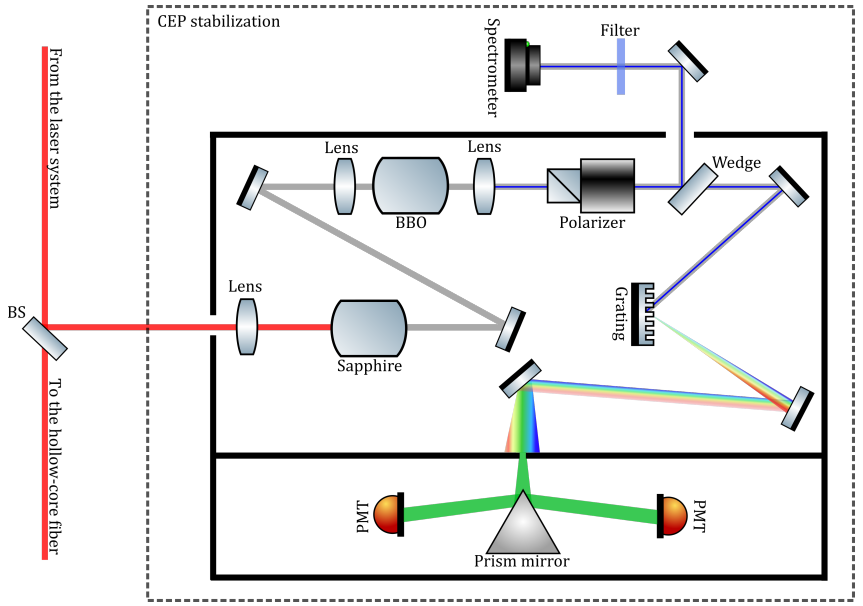

Figure 2.1: Schematic representation of the CEP stabilization module (the so-called BIRD system). The analog loop described in the text uses the error signal measured by the two photomultiplier tubes (PMTs), shown in the lower part of the drawing. The slowest loop exploits the signal coming from the digital spectrometer in the upper part of the drawing.

In our laser system, pulses are CEP-stabilized [68] thanks to three different stabilization stages (summarized in Table 2.2). The first one (Menlo Systems XPS800) is installed just outside the oscillator cavity and consists of a f - f_0 interferometer, able to phase lock the offset frequency at a 1/4 of the oscillator repetition rate, acting in closed loop on an acusto-optic modulator placed in the oscillator pump laser path.

Moreover, in order to correct for the CEP slower frequency

noise generated by the amplification stages, we settled back a high-correction bandwidth feedback loop which was developed in the past in the same laboratory, in collaboration with Amplitude Technologies and CEA-Saclay, the so-called BIRD system [69]. A fully analog f - 2f [70] interferometer is placed at the output of the laser system. A small portion (few μJs) of the beam (see Figure 2.1) is focused onto a 2-mm thick sapphire plate for white light (WL) generation and then focused again by a spherical mirror onto a 50-μm thick barium borate (BBO) crystal for second harmonic generation. The infrared part of the WL is frequency doubled, leading to a new component (2f signal) around 500 nm, perpendicularly polarized with respect to the WL because of type I phase matching. A polarizer then projects the polarization of the two pulses along the same direction, so that interference may occur. The spectral position of the interference fringes is proportional to the CEP offset. A portion of the beam is reflected on a fused silica wedge and collected by a spectrometer. The remaining part of the radiation is diffracted by a grating, that spatially resolves the interference fringes. A single fringe is selected by a slit, separated in two parts by the apex of a reflecting prism, and sent to two photomultiplier tubes (PMTs). Then, on a single shot basis, the outputs of the PMTs are analogically integrated and subtracted, providing an error signal $\Delta\epsilon$ that is proportional to the shot-to-shot variation of the CEP. This signal is then used as input for a proportional-integral (PI) analog feedback loop which acts on an acousto-optic programmable dispersive filter (AOPDF) called Dazzler which is placed in the beam path before the amplification stage. The portion of the radiation

CEP noise type	Solution
Fast CEP noise from the oscillator ($\sim$ 80 MHz).	Menlo Systems XPS800 f - f_0 interferometer + feedback loop on acusto-optic modulator on oscillator pump laser.
Slow frequency noise from amplification stages (10 kHz).	Analog 2 - 2f system (BIRD) + feedback loop acting on the Dazzler.
Very slow varying CEP ($<$ 1 Hz, e.g. due to heating up processes)	f - 2f interferometer (signal taken from BIRD) + digital feedback loop acting on the BIRD controller offset signal.

Table 2.1: Summary of the three CEP stabilization stages.

coming from the f - 2f interferometer and collected by the digital spectrometer is, then, used as an input for the last stabilization loop, which aims to contrast very slow drifts, that take place in several minutes. On a computer, a digital PI controller is implemented on a LabView™ program. The output of this controller acts as an offset signal of the previously described analog controller loop. The combined action of these stabilization loops allowed us to obtain a carrier-envelope phase residual variations contained in a few hundreds of milliradiants (see Figure 2.2).

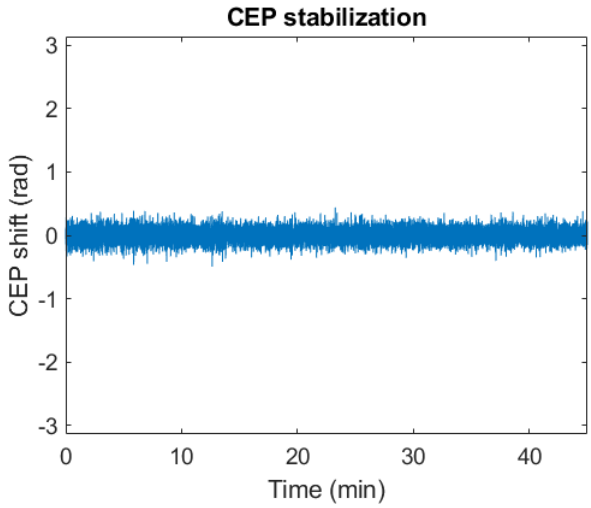

Figure 2.2: CEP stabilization measurement over 45 minutes. The measurement is taken from the phase of the f - 2f interferometer fringes (the BIRD signal, which is the input of the third stabilization stage). The CEP shift is measured every 100 ms giving a residual rms of $\sim$ 110 mrad, and being always less than 440 mrad.

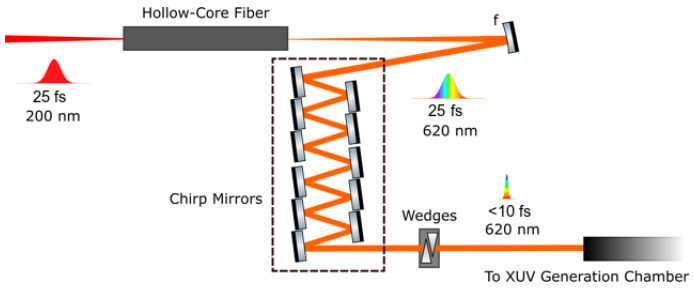

Figure 2.3: Schematic drawing of the hollow-core fiber pulse compression system. Incoming IR pulses are focused in a neon gas filled hollow core fiber. After self phase modulation (SPM) induced spectral broadening, the pulses go through a set of chirped mirrors to compensate for the SPM intrinsic positive dispersion. The last couple of wedge is used to finely adjust the residual dispersion.

2.3 Hollow Core Fiber Compression System

In order to efficiently generate XUV attosecond pulses via HHG, we need few cycle pulses (tipically < 10 fs). 25 fs, thus, is still a too long duration. To further temporally shorten the CEP stabilized pulses, we exploit a hollow core fiber compression system in combination with a battery of chirped mirrors [71] (see Figure 2.3).

The implementation of this setup in our Attosecond Lab has the following parameters: the beam, with an input energy per pulse of ~ 1.6 mJ is focused by a 750 mm focal length spherical mirror into a $\sim$ 1 m long hollow-core fiber (320 μm inner diam-

eter); the resulting spot diameter at focus is $\sim$ 200 μm (65% of the core diameter). The typical output power is 850 μJ; sufficient spectral broadening is obtained with a static neon pressure of about 1.1 bar above the atmospheric pressure. At the output of this stage, the NIR-VIS pulses have a bandwidth ranging between 650 and 1100 nm and a time duration of about 6-7 fs, thus being very close to the transform limit. In Figure 2.4, the laser spectra before and after the hollow core fiber, a FROG trace, acquired after the HCF, and the corresponding retrieved pulse temporal profile, are reported.

2.4 Measurement setup

The compressed pulses enter then the measurement setup composed of three main blocks (see Figure 2.5). The first block consists of an actively-stabilized interferometer, that is able to produce the NIR-VIS pump and the XUV probe pulses with an attosecond adjustable delay. The pulses are subsequently focused on the first target. The second block consists of a noble gas target, placed in correspondence of a TOF spectrometer, and of a refocusing toroidal mirror. The third block is the so-called reflectometer. It contains the solid sample under study, mounted on a roto-translation stage, and a movable golden mirror, which sends the reflected radiation to the XUV spectrometer.

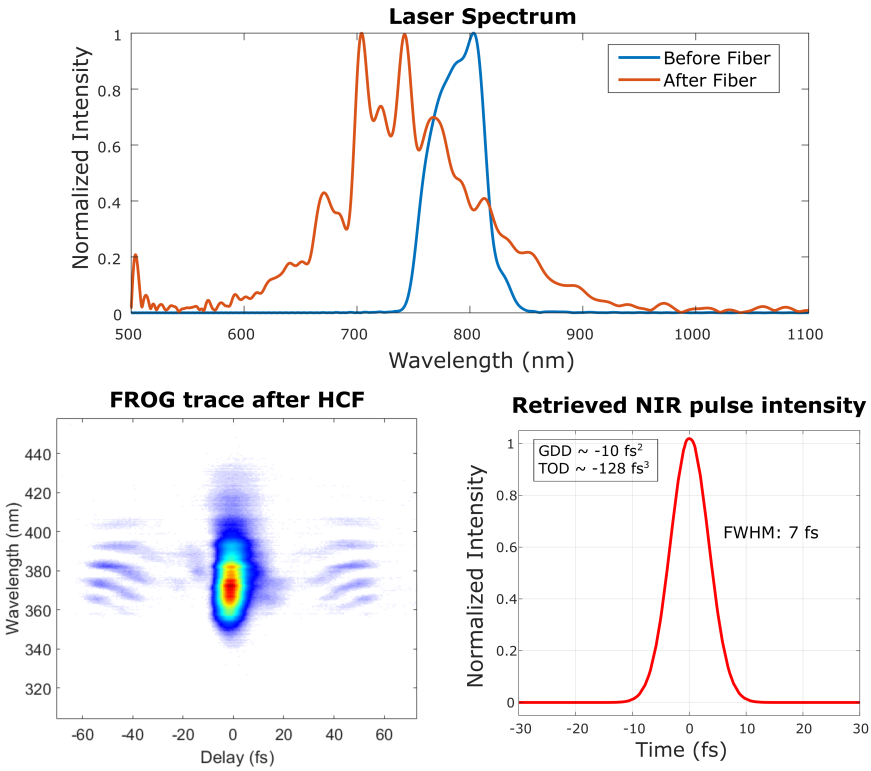

Figure 2.4: Upper panel: Laser spectra before and after HCF. Lower panel: FROG trace acquired after the hollow core fiber, and the retrieved pulse temporal intensity profile.

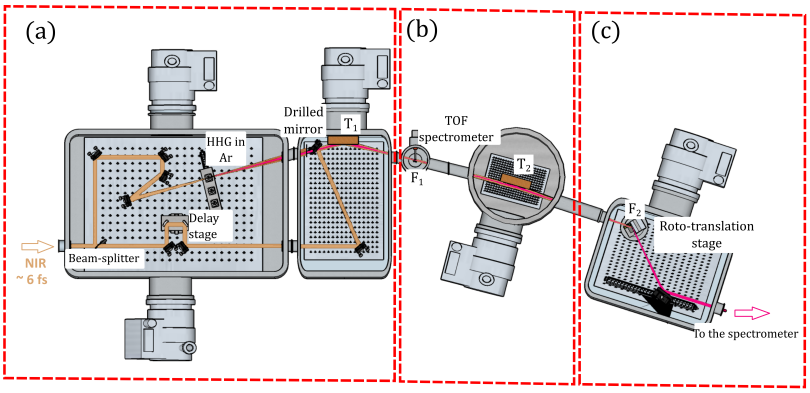

Figure 2.5: Orthogonal projection of the full measurement setup. a) Actively stabilized interferometer. On one arm HHG process takes place. On the other arm a delay stage is set. The collinear recombination of the two paths occurs through a drilled mirror. The two beams are then focused via a toroidal mirror (T_1). b) First focus of the configuration (F_1). A gas target is placed in correspondence to a TOF spectrometer. The beam is then refocused using a second toroidal mirror (T_2). c) Second focus of the configuration (F_2). The solid sample under study is mounted on a roto-translation stage and a movable golden mirror sends the reflected radiation to the XUV spectrometer.

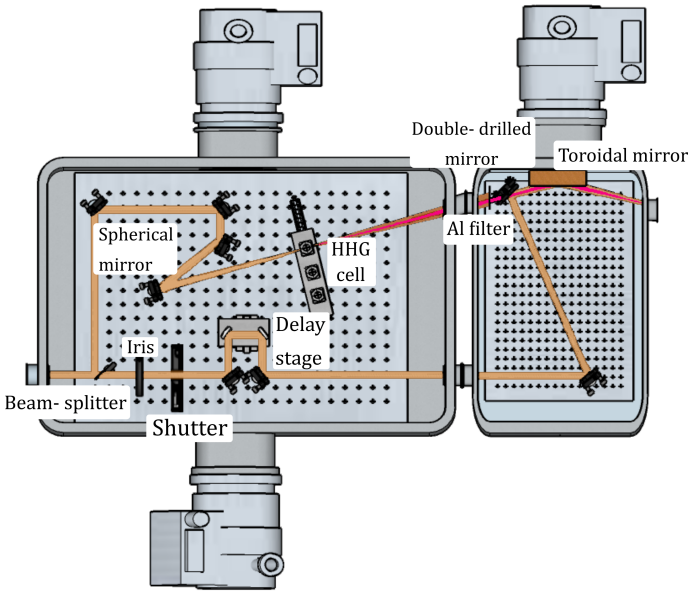

Figure 2.6: Schematic drawing of the Interferometer. NIR-VIS radiation is represented in orange. XUV beam is represented in violet.

2.4.1 Actively-Stabilized Interferometer

The first block of the measurement system is an actively-stabilized interferometer (Figure 2.6) divided in two vacuum chambers.

After entering the first one, through a window at the Brewster angle, the NIR-VIS pulses are split by a 70-30 broadband beam splitter. The reflected part of the IR radiation (70%), with an average energy of $\sim$ 500 μJ per pulse, is focused down to $\sim$ 150 μm by a converging 50- cm mirror onto an argon filled gas

cell. Here High-order Harmonic Generation (HHG) process takes place and XUV attosecond pulses are generated. In our setup, we have three 1-cm thick gas cells, which are essentially three steel parallelepipeds with a through hole (diameter 5 mm), that are connected to a noble gas line. The front and back surfaces of the cells are covered with aluminum tape to separate a region in which high gas density for HHG is present, from the rest of the vacuum chamber. When the laser light is focused onto the cell, it digs two small holes in the tape (entrance and exit one). This is done in order to have the hole as small as possible. The cells are mounted on a motorized XYZ translation stage allowing for proper alignment.

The transmitted part of the NIR-VIS radiation ($\sim$ 300 μJ average energy per pulse), passes first through a motorized iris that can be used to tune the power of the beam. In the path of the NIR-VIS beam is then placed a home-built mechanical shutter. The mechanical design of the shutter is based on the voice-coil actuator used in hard disk drives (HDD) found in common personal computers (see Figure 2.7). On top of the original design extracted from the HDD, a proper casing and electric circuit has been designed as already presented in [72]. This mechanical shutter can be driven at a frequency of 1 Hz for hours without overheating and are thus compatible for operation in vacuum. After that, the beam passes through a delay line formed by a retro-reflector mounted on a translational stage with nanometer resolution (Smaract™ SLC-2445-S-HV). The recombination of the two pulses takes place in the second chamber. A 150- nm thick aluminium filter, mounted on a fused silica support, re-

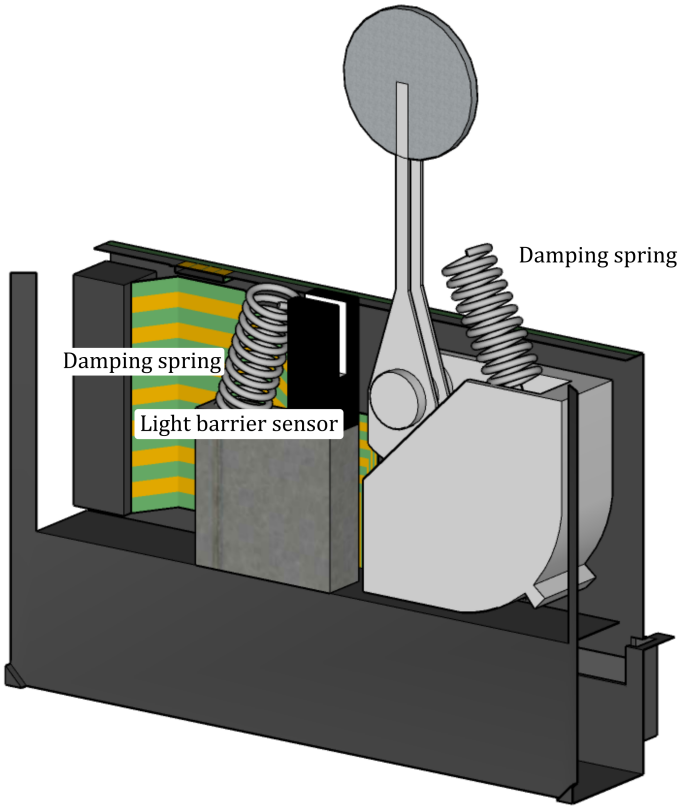

Figure 2.7: Schematic drawing of the home-built shutter used in the experimental setup. Two damping springs are mounted at the sides of the movable hard disk head. A light barrier is placed on one side to give a feedback on the shutter position.

moves the residual IR radiation from the XUV line. After the filter, a double-drilled mirror oriented at 45° both with respect to the XUV line and the IR line is present. The XUV radiation passes through one hole of the mirror, while IR radiation is reflected by the front surface of the mirror. From now on the two beams will propagate collinearly.

In order to perform time-resolved experiments with attosecond resolution, not only the attosecond pulse duration is required, but also a very precise set of the time delay between pump and probe pulse is needed. Any instability and thermal drift can thus be a real problem for the success of the measurement. Active stabilization of the interferometer [73] has been implemented (see Figure 2.8). In this kind of configuration, a stabilized helium-neon (He-Ne) laser beam with a central wavelength of 633 nm enters the other side of the beam-splitter and follows the same optical path of the XUV and NIR-VIS beams up to the double-drilled mirror. On the NIR-VIS side, the He-Ne radiation will go through the motorized iris and the delay stage, while on the XUV side it will be focused through the hole of the gas cell. The spatial divergence of the He-Ne red radiation is larger than the XUV one. Thus, it is not completely blocked by the aluminum filter, passing through the glass support at its side. This part of He-Ne radiation is then reflected by the back of the double-drilled mirror and recombined with the He-Ne radiation which comes from the IR optical path and passes through the second hole of the double-drilled mirror. The spatial interference fringes of these two beams are then measured by a web-cam, that is placed after an optical chopper synchronized with the few-fs pulses, which re-

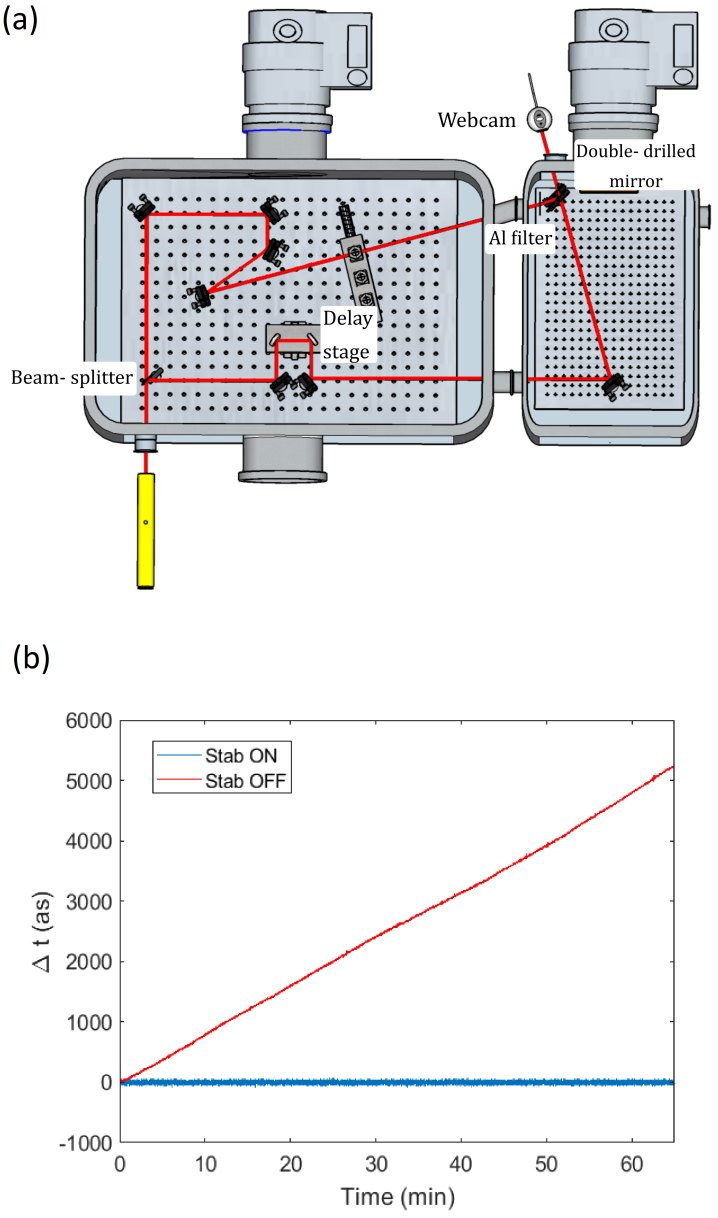

Figure 2.8: (a) Schematic drawing of the He-Ne active stabilization line of the interferometer. (b) Stability measurement over 65 minutes with and without active stabilization. Active stabilization provides a delay stability with a measured r.m.s. of 19 as.

moves the residual NIR-VIS radiation coming at 10 kHz. Using a digital PID controller acting on the delay stage, it is possible to stabilize the position of the fringes (and the length of the arms of the interferometer) and to change the delay in a controlled way.

2.4.2 First Focal Region

After recombination, XUV and NIR-VIS pulses are focused by a gold-coated toroidal mirror (entrance angle $\sim 87°$, focal length 1000 mm) on the first interaction region (see Figure 2.9). It is important to notice that, since the optic is placed 1000 mm from the HHG cell, the focal plane is a 1:1 image of the generation plane. Thus, on the IR side, the collimated IR beam must be reflected by a diverging mirror with a virtual focus that is located at the same distance, from the toroidal mirror, of the HHG cell. The first interaction region is composed by a vacuum chamber in which a needle injects a noble gas jet (in our case, neon) exactly at the focal point of the NIR-VIS and XUV radiation. An electron Time-Of-Flight (TOF) spectrometer (eTOF v6 by Stafan Kaesdorf ™) acquires the XUV photoemitted electron energy spectrum (see an example in Figure 2.9). By varying the delay between XUV and NIR-VIS pulses, these photoelectrons will interact with different regions of the strong NIR-VIS field and experience a momentum shift depending on the ionization time instant [74]. The photoelectron trace, acquired as a function of the XUV-NIR delay, (the so-called streaking trace) is used to characterize both the XUV and IR pulses employed in the experiment and to precisely determine the reciprocal delay between

pump and probe pulses, as we will explain in chapter 3.

After the this first interaction region, a second toroidal mirror (entrance angle $\sim 87°$, focal length 800 mm, 85% reflectivity for s-polarized XUV radiation) collects the radiation coming from this chamber and focuses it once again in the second focal region (see the beam profile of the IR beam in the two focal region in Figure 2.10), where the actual experiments on solids take place.

2.4.3 Second Focal Region

In the second focal region a so-called reflectometer (Figure 2.11) is placed. Here is where the actual attosecond transient reflection spectroscopy experiments are performed. The reflectometer consists of two main elements allowing us to measure the sample reflectance for a wide range of angles of incidence. The first element is a motorized sample holder, providing many degrees of freedom to the sample. The sample can be translated along x, y and z directions thanks to three linear motors (MP-21 by Micronix, with a resolution of 0.1 μm), and rotated around one axis, using a rotor model PR-50SM by Micronix, with a resolution of 10 m°. On the same stage, a golden plane mirror is placed above the sample holder, so that it can be positioned in place of the sample if a sample-free calibration is needed. The sample/mirror holder is shown in Figure 2.12. It is composed by two independent elements, mounted on the same roto-translational stage. The mirror support is simply a piece of steel with a 13-mm grove, designed to hold a gold-coated mirror. The mirror is

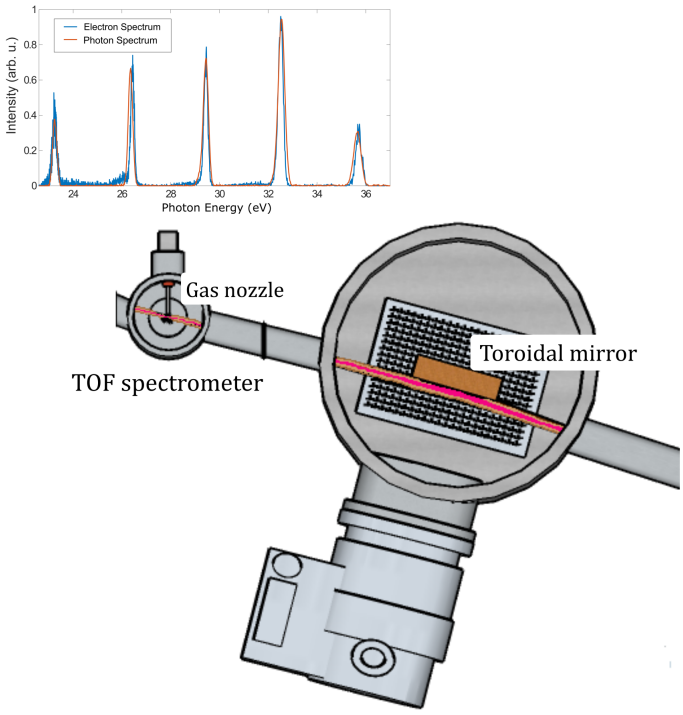

Figure 2.9: Schematic drawing of the first focal region of the measurement setup. In the inset, electron and photon spectra of harmonics, acquired with the present setup, are shown. Harmonics were generated in Ar gas with $\sim$ 25 fs long pulses. Electrons are acquired from photoionization of neon gas (the ionization potential has been summed to the energy axis of the electron spectrum).

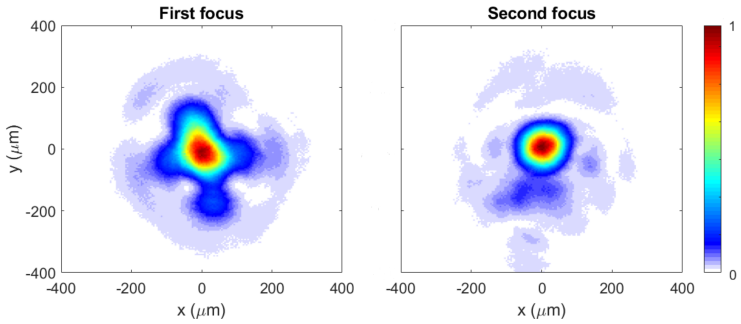

Figure 2.10: Beam profile in the first (left) and second (right) focus of the IR beam.

used, in place of the sample, to collect background or reference data in the experiments. The sample holder is slightly more complex. As no tilt is allowed by the 3D-rototranslator, we designed the sample support to implement manual vertical tilt. When we mount a new sample, we can use a screw to manually adjust the vertical position of the beam reflected by the sample, in order to obtain the same direction as the one reflected by the mirror.

Once the XUV photons interact with the sample and are reflected, they should be directed along a precise direction inside the XUV spectrometer. To do so, a second optical element is used. It is another golden mirror, able to intercept the beam that is reflected by the sample and send it to the spectrometer. In order to run experiments in a wide range of angles of incidence, it is mounted on several motorized supports. First of all, the mirror is inserted in a motorized holder for very fine horizontal and vertical tilt. The holder is placed onto a 360° rotator, similar to the one used in the first stage. The rotator is used

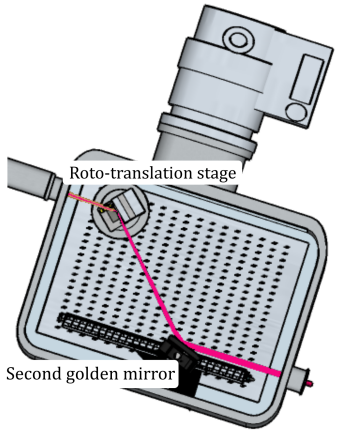

Figure 2.11: Schematic drawing of the second focal region of the measurement setup.

to compensate for the angle variation of the beam propagation direction. Between the mirror holder and the rotator we placed a manual slit, providing a maximum translation of the mirror of about 10 mm. It is used to make sure that the rotation axis is aligned to the mirror surface. Finally, the whole support is mounted to a long-range translator (model MP-21 by Micronix, with a resolution of 0.1 μm), able to shift the mirror for about 200 mm. This is fundamental for intercepting the reflected beam, as even a small variation of the angle of incidence onto the sample may produce a large change in the beam position alongside the propagation direction before the spectrometer. With this kind of system, we can measure sample reflection at any angle, spanning from less than 60° to almost 80°, even in a time-resolved pump-

probe scheme.

The XUV spectrometer has a very simple structure: a diffraction grating (at grazing incidence) spreads the different wavelengths with a known angular separation. In this way photons with different energy hit a space sensitive detector (an MCP) in different positions. Eventually, the electron beam from the MCP is accelerated and then delivered to a phosphorous screen. It converts the kinetic energy carried by the electrons into photons in the visible spectral range via phosphorescence process. A CCD camera collects the image on the phosphorous screen. In order to relate the pixels of the camera to the associated energy (also depending on the diffraction grating used), a calibration procedure is needed. In our typical procedure, we employ radiation coming from empty hollow core fiber to generate the high-order harmonics. Since the absence of the gas prevents the spectral broadening due to the self-phase modulation process, the HHG will give origin to well-separated harmonics at odd multiples of the fundamental frequency of the IR radiation (see the inset of Figure 2.9). Knowing the angular diffraction given by the grating for each energy, it is possible to relate the known energy of the harmonics to the pixels, thus calibrating the XUV spectrometer.

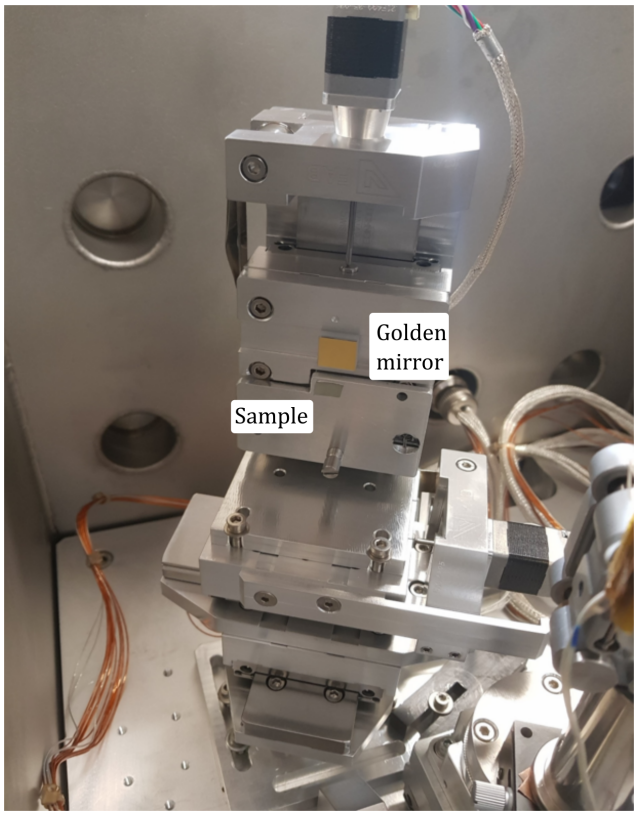

Figure 2.12: Picture of the sample holder mounted on the roto-translation stage. The golden mirror holder is a piece of steel with a groove to accommodate the mirror. The sample holder is a slab to which the sample is glued with silver paste and which allows to vertically tilt the sample by means of a screw.

Chapter 3

Attosecond Core Exciton Dynamics in MgF_2

In this chapter, the very first attosecond transient reflectivity experiment that has been performed using the newly built beamline, aiming at the investigation of the electron dynamics around core excitons in magnesium fluoride, is presented. In the first part of the chapter, I will briefly introduce the theoretical background underlying the experimental work in order to sketch the context in which the experiment is placed. I will then show and discuss the preliminary static reflectivity measurements that we took on the sample. At last, I will describe in detail the pump-probe experiment we performed and discuss the results we obtained.

3.1 Excitons

In semiconductors, dielectrics, clusters, and macromolecules, excitons are quasi-particles defined as bound states between an excited electron from core or valence states and the corresponding hole. In this situation, Coulomb interaction is responsible for their binding energy [75] and, depending on the characteristics of the material that we take into consideration, it is possible to identify two main theoretical models for excitons: the Wannier-Mott excitons and the Frenkel excitons.

3.1.1 Wannier-Mott excitons

A possible theoretical approach to the description of excitons in crystalline solids is the Wannier-Mott one. If we consider a crystal, whose electrical properties are mostly determined by its translation symmetry, we can think of a situation in which the localized electron and hole levels involved in the exciton extend over many lattice constants. One can, then, reasonably approximate the description of their dynamics by means of the conduction and valence band effective masses associated m_e^* and m_h^*, for simplicity considered isotropic. In this picture, these particles will feel an attractive Coulomb interaction that is screened by the collective effect of the other particles of the crystal. The Hamiltonian associated to electrons and holes can be written as:

$$H_e = \frac{\mathbf{p}_e^2}{2m_e^*}, \; H_h = \frac{\mathbf{p}_h^2}{2m_h^*}, \tag{3.1}$$

where $\mathbf{p}_h$ and $\mathbf{p}_e$ are, respectively, the hole and electron mo-

menta. If we now assume to have an interacting electron-hole pair, the whole hamiltonian can be written as:

$$H_{eh} = \frac{\mathbf{p}_e^2}{2m_e^*} + \frac{\mathbf{p}_h^2}{2m_h^*} - \frac{e^2}{4\pi\epsilon|\mathbf{r}_e - \mathbf{r}_h|}, \tag{3.2}$$

where e is the elementary charge, $\mathbf{r}_h$ and $\mathbf{r}_e$ are respectively, the hole and the electron spatial coordinates, and ϵ is the material dielectric constant, taking into account the screening effects. An important assumption in Equation 3.2 is that each particle is producing an external potential for the other, that is not accounted by its effective mass, which is spatially invariant. The Hamiltonian of Equation 3.2, clearly resembles the hydrogen atom one, whose eigenfunctions and eigenvalues are known. We can therefore write a two-particle Schroedinger equation for this system as:

$$H_{eh}\psi(\mathbf{r}_e, \mathbf{r}_h) = \left(-\frac{\hbar^2}{2m_e^*}\nabla^2_{\mathbf{r}_e} - \frac{\hbar^2}{2m_h^*}\nabla^2_{\mathbf{r}_h} - \frac{e^2}{4\pi\epsilon|\mathbf{r}_e - \mathbf{r}_h|} \right) \psi(\mathbf{r}_e, \mathbf{r}_h) = \\ = E_n(K)\psi(\mathbf{r}_e, \mathbf{r}_h), \tag{3.3}$$

where $\nabla^2_{\mathbf{r}_h}$ and $\nabla^2_{\mathbf{r}_e}$ are the Laplace operators applied respectively to the spatial coordinates of the hole and the electron. Assuming zero energy to be placed in the ground state of the crystal without free carriers, defining $M = m_e^* + m_h^*$ as the total mass of the exciton and the reduced mass μ as:

$$\frac{1}{\mu} = \frac{1}{m_e^*} + \frac{1}{m_h^*} \tag{3.4}$$

and transforming the spatial coordinates to describe the position $\mathbf{R}$ of the center of mass of the exciton and the relative position $\mathbf{r}$ between the electron and the hole as:

$$\mathbf{R} = \frac{m_e^* \mathbf{r}_e + m_h^* \mathbf{r}_h}{M}, \mathbf{r} = \mathbf{r}_e - \mathbf{r}_h, \tag{3.5}$$

it is possible to decouple the problem and obtain two equations: one for the center of mass motion, the other for the relative motion of the electron-hole system around the center of mass. The center of mass will behave, then, as a free particle for which we can define a wave vector:

$$\mathbf{K} = \mathbf{k}_e + \mathbf{k}_h, \tag{3.6}$$

and the Schroedinger equation for the quasi-particle will be similar to the hydrogen atom one, which can be solved with the Laguerre polynomials $R_{nl}(r)$ and the spherical harmonic functions $Y_{lm}(\theta, \phi)$. Therefore, the wavefunctions of the exciton can be written as:

$$\psi_{nlm}(\mathbf{R}, \mathbf{r}) = \frac{1}{\sqrt{V}} e^{i\mathbf{K}\cdot\mathbf{R}} R_{nl}(r) Y_{lm}(\theta, \phi), \tag{3.7}$$

where V is the volume in which the exciton is free to move, n is the principal quantum number, l the angular momentum quantum number, and m the magnetic quantum number. The associated energy levels can be written as:

$$E_{nlm} = E_g - \frac{\mu e^4}{2(4\pi\epsilon\hbar)^2} \cdot \frac{1}{n^2} + \frac{\hbar^2 K^2}{2M}, \tag{3.8}$$

where E_g is the material bandgap, the second term is a hydrogen-like attractive energetic term coming from electron-hole Coulomb interaction and the last term is the kinetic energy of the center of mass of the exciton. Here, we can define a *Rydberg constant*

$$G = \frac{\mu e^4}{2(4\pi\epsilon\hbar)^2} \tag{3.9}$$

analogous to the hydrogen atom one, but with the presence of the dielectric constant ϵ as a consequence of the surrounding charges, which makes it typically much smaller than 13.6 eV. The exciton energetic structure, therefore, will result in a hydrogen-like sequence of states slightly below the conduction band edge. It is moreover possible to define an exciton radius, related to the Bohr radius a_0 as:

$$a_{ex} = \frac{4\pi\epsilon\hbar}{\mu e^2} = \frac{m_e\epsilon}{\mu\epsilon_0}a_0 \left(a_0 = \frac{4\pi\epsilon_0\hbar^2}{m_e e^2}\right). \tag{3.10}$$

It is worth noting that this description is simple and intuitive, but it is based on several hypothesis, that may not be satisfied. As an example, if we consider, as unperturbed states, more tightly bound atomic levels, the dielectric constant ϵ of the material will decrease, the reduced effective mass μ will increase and the exciton radius a_{ex} will decrease. Therefore, in this case, the exciton will become more localized and this description will lose its validity; so, different and more complex models may be required to fit the experimental data.

3.1.2 Frenkel excitons

A theoretical model for the description of more localized excitonic states, in particular in molecular, noble gas and ionic crystals, was developed by Frenkel [76] and the quasi-particles that can be well described by this model go under the name of Frenkel excitons. In order to comprehend the formation of these localized excitations, we can start examining how it is possible to generate an excited state from the crystal states. For most purposes, it is not necessary to consider an exciton as being localized, but just as a quantum-mechanical superposition of states. In this light, therefore, excitons are only an expression of the crystal electronic band structure. Let's consider now an insulator in the independent electron approximation. If we move one electron from the valence band to the conduction band, the self-consistent periodic potential will not change in any relevant way: if we put ourselves in the Bloch theorem framework, indeed, the wavefunctions are periodic, the electrons are not localized, and the change in the local charge density will be inversely proportional to the number of atoms in the crystal. The variation is thus extremely small in any macroscopic system. Therefore, the excitation will have an energy E_c - E_v, being E_c and E_v, respectively, the energies associated to the edges of the conduction and valence bands. From a quantum-mechanical point of view, however, there is also another possibility for generate an excited state. Let's assume to superimpose enough levels close to both the minimum of the conduction band and the maximum of the valence band to create two localized wavepackets. In this case, the energy of the populated

wavepacket in the conduction band E_c' will be slightly higher than E_c, while for the valence band the depopulated wavepacket will have an energy E_v' slightly lower than E_v. Thus, the binding energy associated to these localized excitations is, in principle, larger than the delocalized case one. However, if the centres of these two wave packets are spatially close to each other, the electron-electron interaction in the crystal is not negligible anymore and it manifests as an attractive term between the localized conduction band electron and the localized valence band hole. Thus, an additional negative energetic term will have to be considered, and this will make the localized excitation energetically favored. A more quantitative model was reported by Knox [77]. Consider a system with N different atoms: for any of them, it is possible to write the associated time-independent Schroedinger equation to describe its stationary states as:

$$H_0(\mathbf{r})\phi_n(\mathbf{r}) = E_n\phi_n(\mathbf{r}). \tag{3.11}$$

Here, we can assume that all the ground state atoms of the system, whose position will be indicated by the coordinate $\mathbf{R}_I$, will contribute to generate a set of unperturbed states identified by the following eigenvalue equation:

$$H_{0,I}(\mathbf{r}-\mathbf{R}_I)\phi_{I,n}(\mathbf{r}-\mathbf{R}_I) = E_{I,n}(\mathbf{r}-\mathbf{R}_I)\phi_{I,n}(\mathbf{r}-\mathbf{R}_I), \tag{3.12}$$

where $\mathbf{r}$ is the coordinate associated to all the degrees of freedom of the atom, n is the set of quantum numbers of the system,

and I indexes the generic lattice site[1]. Equation 3.12 includes the effect of the whole crystal on a specific lattice site as an effective potential included in the unperturbed site-dependent hamiltonian $H_{0,I}$. A common assumption, at this point, is that all the N atoms in the crystal are independent, with additional effects associated to phonon interactions and physical differences between lattice sites. This approach is not suitable to describe excitons because interaction between the excitations and the lattice sites are fundamental. If we consider e being the elementary charge, ϵ_0 the electric constant of vacuum and Z_I the atomic number of the I-th site, for a fixed configuration of the nuclei, we can write the Hamiltonian of this many-body problem by summing the kinetic energy of electrons, the Coulomb interaction between nuclei and electrons, the Coulomb interaction between nuclei, and the Coulomb interaction between electrons as:

$$H = \sum_i \frac{\mathbf{p}_i^2}{2m} - \sum_{i,I} \frac{Z_I e^2}{4\pi\epsilon_0 |\mathbf{R}_I - \mathbf{r}_i|} + \sum_{I<J} \frac{Z_I Z_J e^2}{4\pi\epsilon_0 |\mathbf{R}_I - \mathbf{R}_J|} + \\ + \sum_{i<j} \frac{e^2}{2\pi\epsilon_0 |\mathbf{r}_i - \mathbf{r}_j|}, \quad (3.13)$$

where $\mathbf{p}_i$ is the i-th electron momentum. We can split this Hamiltonian in a sum of terms associated to the already defined crystal field Hamiltonian $H_{0,I}$ and in a sum of terms accounting

[1] In the adopted convention, capital letters indexes the nuclei, while lowercase letters are associated to electrons

for the site to site interaction:

$$H = \sum_I H_{0,I} + \sum_{I<J} V_{I,J}. \tag{3.14}$$

This splitting is not trivial, actually. Part of the inter-site interactions, indeed, are already present in the first summation and, therefore, the second one must be written in a way to avoid duplicating terms associated to these interactions. Moreover, indistinguishability of electrons and the associated exchange interactions must be considered. Frenkel's approach is to write the ground state wavefunction for the crystal as the product of the antisymmetrized ground-state crystal field wavefunctions

$$\Phi_0 = \phi_{1,0} \cdot \phi_{2,0} \cdot ... \cdot \phi_{I,0} \cdot ... \tag{3.15}$$

and the excited state of the system as the same product in which the crystal field function of the I-th lattice site is excited

$$\Phi_{I,n} = \phi_{1,0} \cdot \phi_{2,0} \cdot ... \cdot \phi_{I,n} \cdot .... \tag{3.16}$$

Without any interaction between the different lattice sites, the wave function $\Phi_{I,n}$ will have a degeneracy equal to the number of lattice sites that are present in the crystal. Anyway, since we have considered that this excitation can be transferred between neighboring lattice sites, there will be matrix elements of the kind $\langle \Phi_{I,n} | H | \Phi_{J,n'} \rangle$, that are different from zero even if $I \neq J$. This is the most peculiar characteristic of Frenkel excitons. If now we assume that the interaction is present only between neighboring lattice sites and that $n = 1$, then, the complete Schroedinger

equation associated can be written as:

$$H\Phi_{I,1} = E_{I,1}\Phi_{I,1} + V_{I,I\pm1}(\Phi_{I-1,1} + \Phi_{I+1,1}) \tag{3.17}$$

where $V_{I,I\pm1}$ is accounting for the inter-sites interaction energy. In this case, clearly, the wavefunctions $\Phi_{I,1}$ are not eigenvalues of the Hamiltonian; the diagonalization of this operator brings then to a new set of eigenstates for the system. In the simplified case of a linear, monodimensional lattice of atoms with a lattice constant a, these eigenfunctions can be written as[2]:

$$\Psi_K = \sum_I e^{iIa\cdot K}\Phi_{I,1} \tag{3.18}$$

where K is the quantum number of the expansion. It is easy to foresee that $\hbar K$ will be the quasi-momentum of the exciton. So, the Schroedinger equation of this system will become:

$$\begin{aligned} H\Psi_K = \sum_I e^{iIaK}[E + V(e^{-iaK} + e^{iaK})]\Phi_{I,1} = \\ = [E + 2V\cos(Ka)]\Psi_k = \mathcal{E}(K)\Psi_K \end{aligned} \tag{3.19}$$

where we considered $E_{I,1} = E, V_{I,J} = V \;\forall\; I, J = I \pm 1$.

So, in this case, the quasi-momentum K of the exciton will be considered as a quasi-continuum variable within the first Brillouin zone and the presence of the lattice site coupling V will just broaden the excitation energies into a band. The dispersion

[2]From now on i is the imaginary unit.

relation of this particle will therefore be:

$$\mathcal{E}(K) = E + 2V\cos(Ka) \tag{3.20}$$

and it is possible to calculate the effective mass of the exciton as:

$$M^* = \hbar^2 \left(\frac{\partial^2 \mathcal{E}(K)}{\partial K^2} \right)^{-1} = -\frac{\hbar^2}{2a^2 V}\cos(Ka). \tag{3.21}$$

From an energetic point of view, the effect of the exciton presence will be to eliminate the degeneracy of the states involved, forming a band that will have an energy width of $4V$.

3.1.3 Core excitons

Frenkel and Wannier-Mott methods for exciton description are limiting cases of the same, unified approach [77]. From a general point of view, the whole problem reduces to the definition of a crystal Hamiltonian, choosing a suitable representation spanning all the interesting states of the system. Then, by diagonalizing this Hamiltonian: one can find the associated eigenstates, that will be the exciton states. Obviously, the choice of the initial representation may ease the problem, if it is based on a prior knowledge of the molecules or atoms involved. Specifically, the knowledge of the dielectric constant, the crystalline order, the size of the band-gap, and the Coulomb interaction can help for this choice. That is why, for Wannier-Mott excitons, we started our discussion from the description of free carriers, while for Frenkel

excitons we used localized functions. Excitons in ionic crystals (as magnesium fluoride) have large binding energies [77]. In this case, it is usually possible to use the Frenkel model, being particularly careful in considering the localization of this excitation on the ionic species, that may sometimes lead to intermediate descriptions between the Wannier-Mott and Frenkel models. From a qualitative point of view, the core hole is strongly localized, and thus it is possible to interpret a core exciton as an electron-hole pair excited state where the hole is massive enough to remain trapped on the same excited atom during the whole lifetime of the exciton [78]. Also from a theoretical approach, their characteristics are neither completely captured by the Frenkel model, since the local environment of the core hole is strongly influent, nor by the Wannier-Mott model, since the short-range core-hole interaction cannot be neglected and the localization of the atomic states involved makes almost impossible, for core excitons, to hop to neighbouring atomic states. Possible theoretical interpretations of experimental results for core excitons, either starting from the Frenkel representation [78], or from the Wannier-Mott one [79], have been proposed, but the only possibility to really describe them properly, seems to be ab initio calculations [80].

3.2 Magnesium Fluoride

Magnesium fluoride (MgF_2) is an insulator belonging to the family of the alkaline-earth fluorides. At ambient conditions, it is a crystal and it has a rutile structure, with space group D_{4h}^{14}.

Its unit cell is a simple tetragonal and comprehend six ions: two Mg^{2+} and four F^{-}. It is a strongly ionic solid: when the solid crystal structure is arranged, two electrons are transferred from the *s* states of metal atoms to the *p* states of fluorines. The electronic band structure of magnesium fluoride was calculated by Jouanin *et al.* [81] using a combined tight binding and pseudopotential method starting from numerous experimental data (see Figure 3.1). They reported that the wavefunctions of the deep ionic states of the two atomic species involved in the crystal are localized and therefore their contribution to the higher valence bands is negligible. Due to the complicated crystal structure, involving six ions per unit cell, a large number of bands is present, with degeneracies at the boundaries of the Brillouin zone due to the crystal symmetry. The highest point of the valence bands is in the Γ point, at the centre of the Brillouin zone, and it is associated to a band rising from a mixing of the $2p_z$ orbitals of the fluorine atoms. The wavefunctions associated to the minimal energy conduction band, instead, are mainly related to the s states of the magnesium atoms. The minimum of these bands is again in the Γ point, which means that magnesium fluoride is a direct bandgap insulator. It is also reported that a shift towards higher energies of the valence band and towards lower energies of the conduction band is expected as a consequence of polarization corrections as further confirmed by Scrocco [82]. This allows for a better interpretation of the experimental optical spectra reported by Hanson *et al.* (reflectivity spectrum, see Figure 3.2) [1] and Rabe *et al.* (absorbance) [83]. In these experiments, it is particularly interesting to notice the presence of a peak in the ab-

sorption/reflection around 54.6 eV photon energy, attributed by Jouanin *et al.* [81] to the presence of semi-core excitonic states, excited from the 2p state of magnesium. The onset of the interband transitions of the 2p bands of the Mg^{2+} ion is indeed located at 56 eV.

To conclude, in an experiment employing broadband XUV spectrum, we expect to be able to address, starting from MgF_2 $2p$ semicore states, the bottom of the conduction band of the unperturbed material, located around 56 eV, the top of the unperturbed valence band around 43.2 eV (assuming the band gap to be equal to 12.8 eV, as reported in [82]) and the core exciton peaks around 54.6 eV.

3.3 Static Reflectivity Measurement

An important preliminary study, before the investigation of temporal dynamics, is the analysis of the static reflectivity of the material. In this section, I will present the method that we used to measure the static reflectivity with our setup and I will show its application to the analysis of the static reflectivity of magnesium fluoride. Finally, I will present the analysis we performed to determine the best angle for the transient reflectivity study.

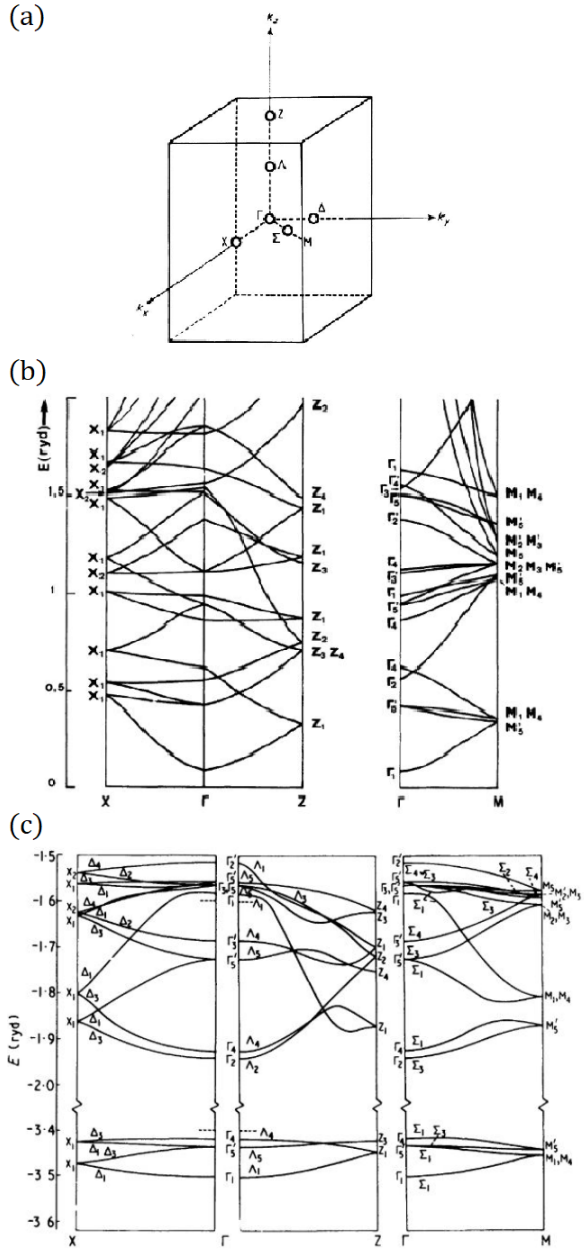

Figure 3.1: Calculated band structure of MgF_2 from [81]. (a) MgF_2 Brillouin zone (simple tetragonal lattice). (b) Calculated conduction band of MgF_2. (c) Calculated valence band of MgF_2.

3.3.1 Theoretical Background

From classical physics, the electric field reflected by a surface can be written, as a function of the incident electric field as:

$$E_r = rE_i \tag{3.22}$$

where, E_r is the reflected electric field, E_i is the incident electric field and r is the reflection coefficient. The reflection coefficient can be written in two different ways as a function of the polarization (s or p) of the incident light, thanks to the Fresnel equations:

$$r_s = \frac{\tilde{n}_1 \cos(\theta_i) - \tilde{n}_2 \sqrt{1 - (\frac{\tilde{n}_1}{\tilde{n}_2} \sin(\theta_i))^2}}{\tilde{n}_1 \cos(\theta_i) + \tilde{n}_2 \sqrt{1 - (\frac{\tilde{n}_1}{\tilde{n}_2} \sin(\theta_i))^2}} \tag{3.23}$$

$$r_p = \frac{\tilde{n}_2 \cos(\theta_i) - \tilde{n}_1 \sqrt{1 - (\frac{\tilde{n}_1}{\tilde{n}_2} \sin(\theta_i))^2}}{\tilde{n}_2 \cos(\theta_i) + \tilde{n}_1 \sqrt{1 - (\frac{\tilde{n}_1}{\tilde{n}_2} \sin(\theta_i))^2}} \tag{3.24}$$

where θ_i is the angle of incidence of incoming radiation with respect to the normal to the surface and $\tilde{n}_1$ and $\tilde{n}_2$ are the complex refractive indexes of the two materials involved in the reflection process

$$\tilde{n}_1 = n_1 + ik_1 \tag{3.25}$$

$$\tilde{n}_2 = n_2 + ik_2 \tag{3.26}$$

$\tilde{n}$ can be also defined as a function of the complex dielectric

constant of the material ϵ as

$$\tilde{n}^2 = \epsilon = \epsilon_1 + i\epsilon_2. \tag{3.27}$$

It is possible, moreover, to define intensity reflection coefficients (or reflectance) as

$$R_s = |r_s|^2 \tag{3.28}$$

$$R_p = |r_p|^2. \tag{3.29}$$

3.3.2 Static Reflectivity of Magnesium Fluoride

The idea of testing the electron dynamics around core excitons in magnesium fluoride comes from the fact that in 1972 Hanson *et al.* [1] reported some static reflectivity measurements at an incidence of 15° from the normal in the XUV spectral range on MgF_2 that showed a very evident peak around 54.6 eV, which was interpreted as due to an exciton interaction (see Figure 3.2) coming from excitation of Mg^{2+} 2p core states (as suggested in [83]). The first step of our study, then, was to repeat this static measurement with our setup.

Due to the geometry of the setup, it is not possible to directly measure the reflectivity of the sample, since a further reflection of the golden mirror is always needed for the radiation to reach the XUV spectrometer. To correctly measure the reflectance of the sample, then, some additional analysis is required. In particular,

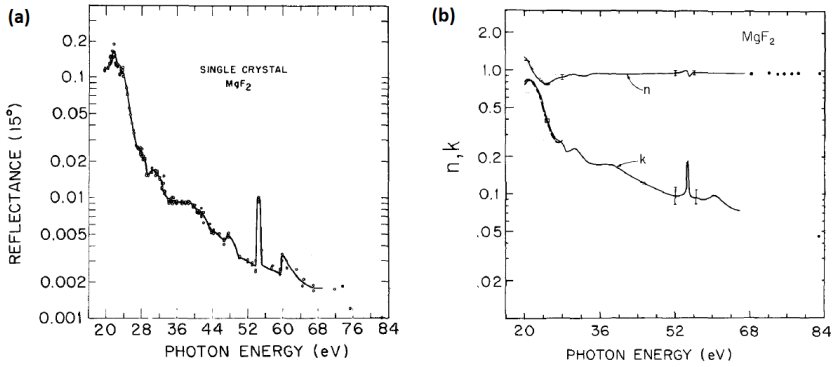

Figure 3.2: (a) Near-normal (15°) reflectance of single-crystal MgF_2 vs. incident photon energy as measured by Hanson *et al.*. (b) Optical constants of MgF_2 vs. incident photon energy as measured by Hanson *et al.*. Figure adapted with permission from [1].

the reflectance of the second mirror must be taken into account. Being I_0 the input XUV intensity for a given wavelength to the reflectometer, the measured intensity at the same wavelength in the spectrometer will be:

$$I_{m,s} = R_g R_s I_0 \tag{3.30}$$

where R_g is the gold reflectance, and R_s is the desired sample reflectance. Thus, it is not possible to directly assess the sample reflectance by a single measurement since we have no information about I_0. An additional measurement is required as reference. To do so, in general, we use another golden mirror in place of the sample, so that we can measure:

$$I_{m,Ref} = R_g R_g I_0 \tag{3.31}$$

If we then divide $I_{m,s}$ by $I_{m,Ref}$, we can obtain:

$$\frac{I_{m,s}}{I_{m,Ref}} = \frac{R_s}{R_g} \tag{3.32}$$

To extract the information on the sample reflectance, absolute data about gold reflectance are then needed. Since gold is a noble metal, which does not degrade easily even if exposed to air, we decided to use tabulated values for the reflectance of such material from the Center for X-Ray Optics (CXRO) website.

In the case of magnesium fluoride, to be even more precise in the static measurement of the reflectivity, we used, as golden mirror, a layer of 50 nm of gold, directly deposited to one side the

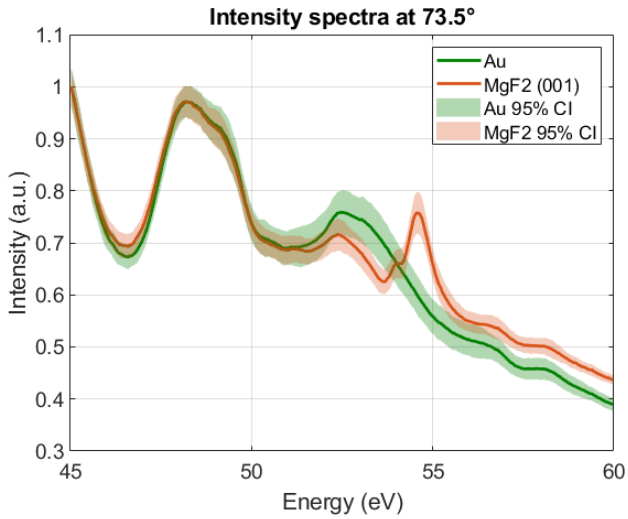

Figure 3.3: Comparison between the measured photon spectrum after reflection on magnesium fluoride and on the golden mirror and after reflection on the two golden mirrors at 73.5°. Confidence intervals are calculated over 10 measurements.

sample. In this experiment, we measured the sample static reflectivity of two different crystal cuts, (001) and (110) at different angles of incidence. The results are shown in Figure 3.4.

In Figure 3.5, I show the comparison between the static reflectivity measured with our setup at 73.5° and the static reflectivity calculated from the optical constants n and k reported in Hanson's paper. It is interesting to notice that, due to the very poor spectral resolution of Hanson's measurements (about 1.3 eV), the excitonic peak seems to be slightly shifted toward lower energies. Interestingly, in our case (XUV spectrometer resolution $\sim$ 0.03 eV), we can resolve also the presence of two peaks. This indicates the presence of two excitonic states A and B coupled to the s-symmetric minimum of the conduction band, which is formed by 3s-states of Mg^{2+}, as suggested in 1972 by Rabe *et al.* [83] from the analysis of experimental MgF_2 absorbance data. It is difficult to define the correct energy position and width of A and B peaks since the strong background in MgF_2 reflectance prohibits to fit the data with any of the usual curves (gaussian, lorentzian). It is anyway evident that the energy separation of the two peaks is at least below 0.6 eV, clearly below Hanson's experimental resolution. This observation validates our approach to measure static reflection.

3.3.3 Angle Determination for Time-Resolved Experiment

A relevant decision, in a transient reflectivity spectroscopy experiment, is the choice of the incidence angle between the in-

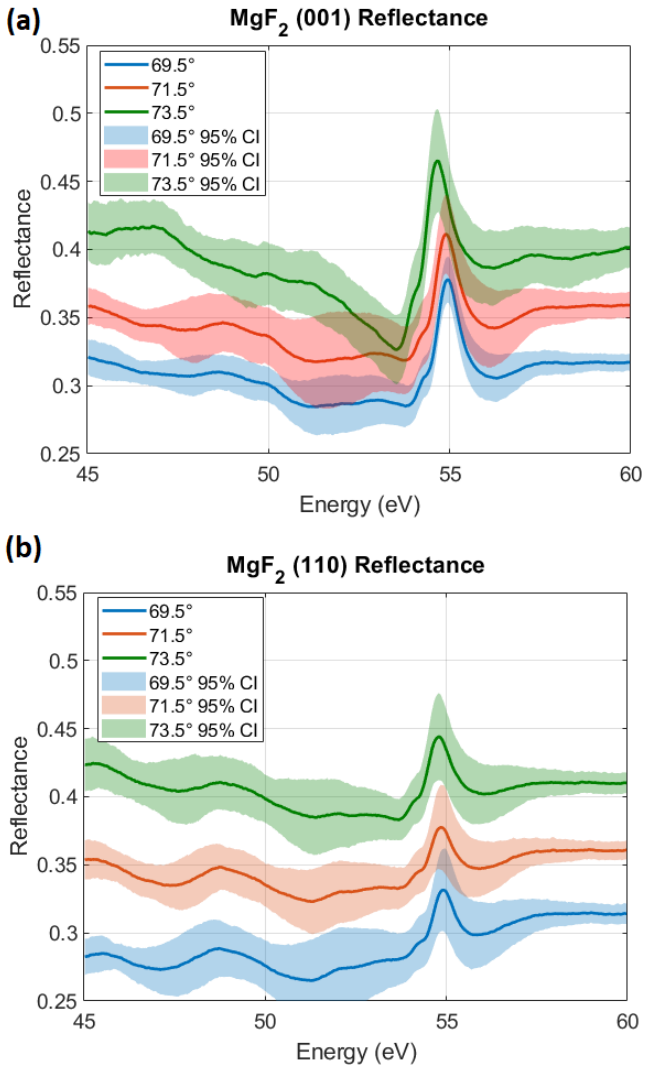

Figure 3.4: (a) Static reflectivity of MgF_2 (001) as a function of the incidence angle. (b) Static reflectivity of MgF_2 as a function of the incidence angle. Confidence intervals are calculated over 10 measurements.

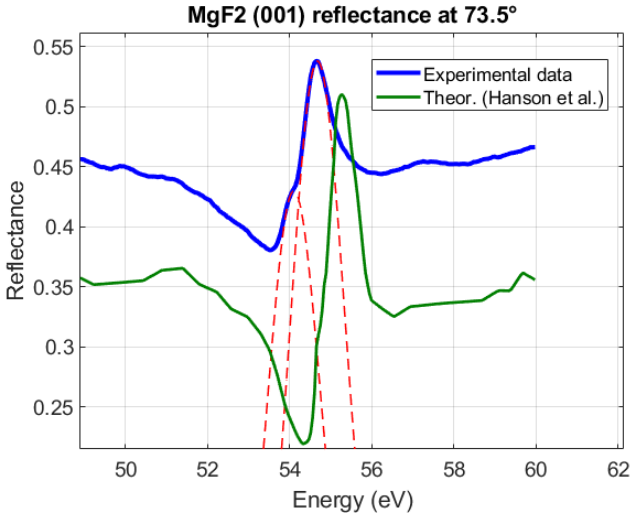

Figure 3.5: Static reflectivity of MgF_2 (001) measured with our setup compared with static reflectivity of MgF_2 (110) calculated from Hanson's optical constants. Red dashed line are guide for the eyes to localize the two excitonic peaks in the measured data.

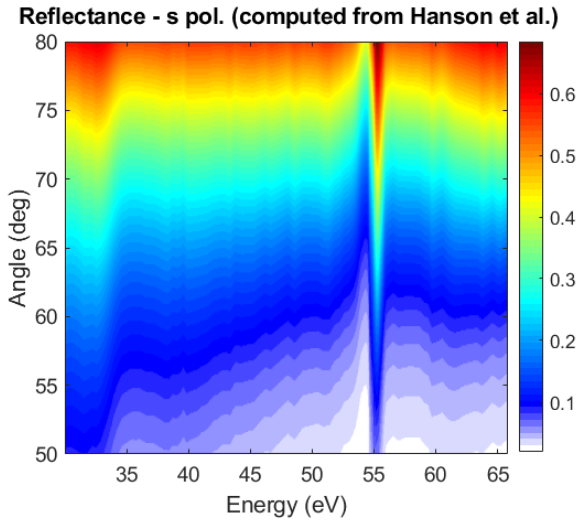

Figure 3.6: Calculated static reflectance of magnesium fluoride for incident angles ranging from 50° to 80° by exploiting Fresnel equations using the numerical values for the complex refractive index reported by Hanson *et al.* [1] as input.

coming pump-probe radiation and the normal to the surface of the sample.

One possible criterion for the determination of the experimental angle is the possibility to partially disentangle the contribution to the reflectivity variation given by the real part of the material dielectric constant ϵ_1 (mainly related to the phase shift of the electric field due to the reflection) and its imaginary component ϵ_2 (mainly associated to the absorption of the incoming radiation) as reported in [20]. We calculated the static reflectance of magnesium fluoride for incident angles ranging from 50° to 80° by exploiting equations 3.23 and 3.28 with the numerical values

for the complex refractive index reported by Hanson *et al.* [1] (Figure 3.6). If we derive this expression with respect to the imaginary part of the dielectric constant of the material (ϵ_2, considering an interface between vacuum (whose refractive index is one) and magnesium fluoride, we obtain:

$$\frac{R_s}{\epsilon_2} = 2\Re\left(r_s^* \cdot \frac{r_s}{\epsilon_2}\right),$$
$$\frac{r_s}{\epsilon_2} = \frac{1}{[\sqrt{\tilde{n}^2 - \sin^2(\theta_i)} + cos(\theta_i)]^2} \cdot \frac{i\cos(\theta_i)}{2\sqrt{\tilde{n}^2 - \sin^2(\theta_i)}} \quad (3.33)$$

with the same notation previously adopted. It is therefore possible to compute those angles at which the dependence on the imaginary part of the complex dielectric function of the material is minimized. Figure 3.7 displays the derivative of the reflectivity of magnesium fluoride with respect to ϵ_2 as a function of the incidence angle θ_i and of the photon energy. The dashed line connects all those points in which the derivative is zero. The angle for which $\frac{R_s}{\epsilon_2}$ is zero at the exciton energy region ($\sim$ 54.6 eV) is around 73.5°.

Another possible decision is to set the incidence angle equal to the critical angle for total internal reflection. For an interface between a given material of refractive index n_1, and another material of lower index n_2, there exists a critical angle of incidence

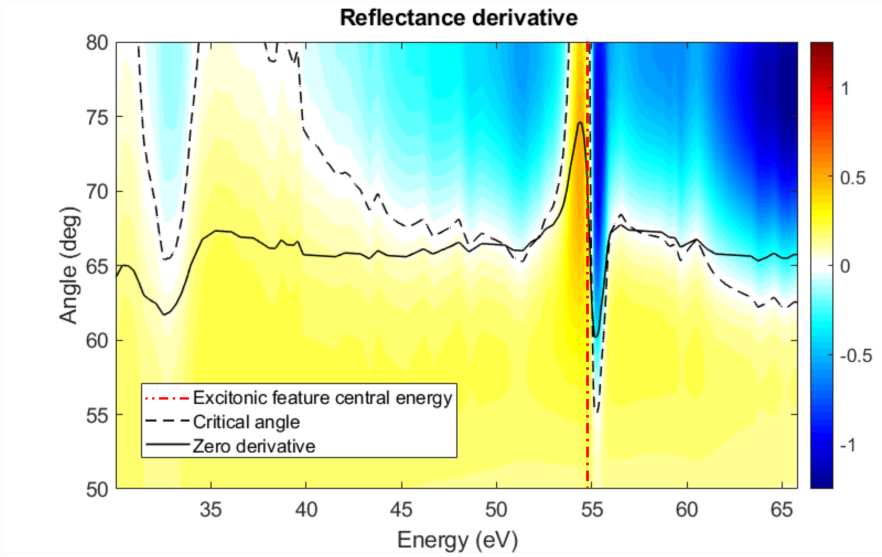

Figure 3.7: Derivative of the reflectivity of magnesium fluoride with respect to the imaginary part of the complex dielectric function ϵ_2. Black solid line indicates the angle for total internal reflection. Black dashed line connects all those points in which the derivative is zero. Red dash-dotted line indicates the central energy position of the excitonic feature.

θ_{crit}, defined as:

$$\theta_{crit} = \arcsin\left(\frac{n_2}{n_1}\right) \tag{3.34}$$

At and beyond this angle of incidence any incident light will be totally internally reflected. However, there is still an electric field above the surface, which falls off exponentially along the z-axis, called evanescent field. The existence of the evanescent field can be found theoretically by the derivation of the Fresnel transmission coefficients:

$$t_s(k_x, k_y) = \frac{2\mu_2 k_{z1}}{\mu_2 k_{z1} + \mu_1 k_{z2}} \tag{3.35}$$

$$t_p(k_x, k_y) = \frac{2\epsilon_2 k_{z1}}{\epsilon_2 k_{z1} + \epsilon_1 k_{z2}} \sqrt{\frac{\mu_2 \epsilon_1}{\mu_1 \epsilon_2}}. \tag{3.36}$$

In these equations k_{z1} and k_{z2} are the components of the wavevectors in the two media along the z axis. The x and y components of the wavevector are conserved across the boundary, hence the z components relate to them as follows:

$$k_{z1} = \sqrt{k_1^2 - (k_x^2 + k_y^2)} \qquad k_{z2} = \sqrt{k_2^2 - (k_x^2 + k_y^2)} \tag{3.37}$$

Where k_1 and k_2 are the magnitudes of the wavevector before and after the interface respectively. For our purposes, it is more convenient to describe these in terms of the angle of incidence θ_i, rather than the other wavevectors. So, if we express the transverse wavenumber as $k_{trans} = \sqrt{k_x + k_y} = k_1 \sin\theta_i$, we can

write:

$$k_{z1} = k_1\sqrt{1-\sin^2\theta_i} \qquad k_{z2} = k_2\sqrt{1-n_r^2\sin^2\theta_i} \tag{3.38}$$

where n_r is the relative index of refraction. The expression for θ_{crit} comes directly by equating the square root argument in the equation for k_{z2} to zero. It is clear from this that, while it is indeed zero at the critical angle, after that k_{z2} becomes imaginary, leading to the evanescent wave.

If we simulate the behavior of the squared modulus of the transmission coefficient for given parameters as a function of the angle of incidence [84] (Figure 3.8), we can see that there is a big field enhancement in correspondence of the critical angle. One can, then, take advantage of this near-field enhancement, in order to have an augmented field effect on the sample. Solid line in Figure 3.7 represents the critical angle in MgF_2 as a function of the photon energy, it is possible to notice that, in the energy region associated to the excitonic peak, the critical angle quite closely tracks the dashed line, further confirming the choice of an incidence angle of 73.5° for the transient reflection spectroscopy experiment.

3.4 ATRS Experiment Description

The experiment that we performed on MgF_2 is an attosecond transient reflectivity spectroscopy experiment. The XUV attosecond (probe) pulse spectrum reflected from the sample in presence

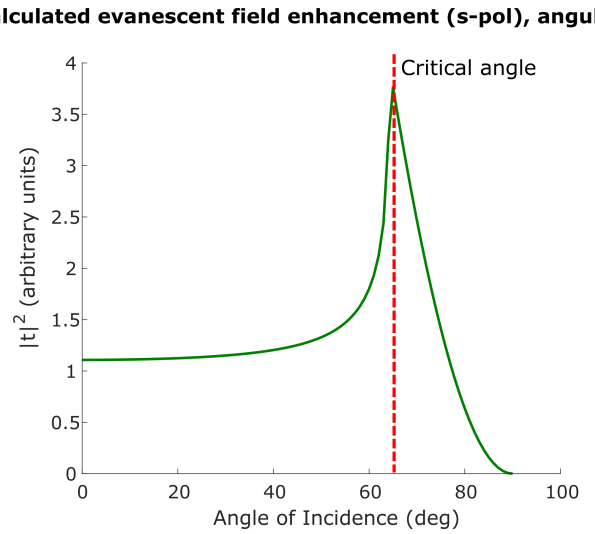

Figure 3.8: Squared modulus of the transmission coefficient for arbitrary parameters as a function of the angle of incidence, for s-polarized light (see Equation 3.35).

of an intense $\sim$ 6-fs NIR-VIS pump pulse is compared with the same spectrum measured in absence of the NIR-VIS pulse for a number of reciprocal delays between pump and probe. If we define: $S(\Delta\tau, E)$, as the XUV photon spectrum reflected by the sample when the NIR-VIS pulse is present and $S'(E)$ as the same spectrum acquired when the pump pulse is off (where $\Delta\tau$ is the temporal delay between the peak intensity of the XUV single attosecond pulse and the peak intensity of the NIR-VIS pulse and E is the energy of the XUV photon), the differential reflectivity signal, for a given delay $\Delta\tau$ and XUV photon energy E, is given by:

$$\frac{\Delta R}{R}(\Delta\tau, E) = \frac{S(\Delta\tau, E) - S'(E)}{S'(E)} \tag{3.39}$$

From a practical point of view, therefore, two different sets of XUV photon spectra are acquired and averaged for every delay: one in presence of the NIR-VIS pulse, the other blocking the pump side of the interferometer by means of a shutter driven at a frequency of 1 Hz (see Figure 2.7). The plot with all the measured delays on the x axis, the photon energy on y axis and $\frac{\Delta R}{R}(\Delta\tau, E)$ on z is called transient reflectivity trace.

The main advantage of having the two-foci experimental setup described in Chapter 2, is the possibility to run two different experiments at the same time. By placing a gas target in the first focus, it is possible to acquire a photoelectron streaking trace in the TOF spectrometer, while acquiring a transient reflectivity trace in the second focus. The streaking trace can be used to

retrieve the exact temporal shape of both the XUV and the NIR-VIS pulses acting on the solid sample by applying an iterative algorithm such as PCGPA [38] (the most widely used), LSGPA [39] and ePIE [41] (see Section 1.1.2). At the same time, the photoelectron trace can work as a reference for the delay axis for the transient reflectivity trace. In fact, it is possible to extract, from the streaking energy center of mass, the behavior of the vector potential of the NIR-VIS pulse exactly in the place where the trace is acquired. It is thus needed, in order to know the exact field acting on the sample, to make a calibration measurement in order to take into account the phase accumulation due to the refocusing process.

3.5 Experimental Results

In this section, the experimental results of the first attosecond transient reflectivity experiment performed using our newly built setup are reported. In Figure 3.9, we show the two experimental traces, simultaneously acquired in the two foci. In the left panel, the photoelectron streaking trace acquired in Ne with an acquisition time of 120 s per delay is reported. In the right panel, we show $\Delta R/R$ as a function of photon energy and pump-probe delay. For each delay step, we averaged over 120 different spectra with and without the NIR-VIS pump pulse. Each spectrum was obtained with an exposure time of the CCD camera of the XUV spectrometer of 0.1 s. Furthermore, in order to re-

move high frequency noise, we applied a low pass filter (cutoff frequency = 1 PHz) line by line. The delay steps for the acquisition of both traces is of 0.25 fs. The chosen delay convention is: positive delays means NIR-VIS pulse comes first. The peak intensity of the near-infrared pump pulse was of $(1.32 \pm 0.07) \times 10^{13}$ W/cm^2. In the following subsections, we will discuss how the photoelectron trace has been used to calibrate the delay axis and to characterize the NIR pulses and the isolated attosecond pulses involved in the experiment. Then, an analysis of the transient reflectivity trace will be presented.

3.5.1 Pulse characterization

As already mentioned in this thesis, it is possible to completely reconstruct both the NIR-VIS pulses and the XUV single attosecond pulses involved in the pump-probe experiment by means of an iterative reconstruction algorithm. The reconstruction algorithm that is adopted in this work is called extended Ptychographic Iterative Engine (ePIE) [85, 86]. It is derived from a reconstruction scheme for lensless imaging, where the far-field diffraction pattern of an object illuminated by a coherent beam is measured for different positions of the light source. The information coming from different and partially overlapping regions can be used to reconstruct the object. A major advantage of this algorithm is that it is also able to reconstruct both the image and the characteristics of the illuminating beam. If we consider the photoelectron spectra as diffraction patterns, the NIR dressing field as the coherent illuminating beam and the XUV attosecond

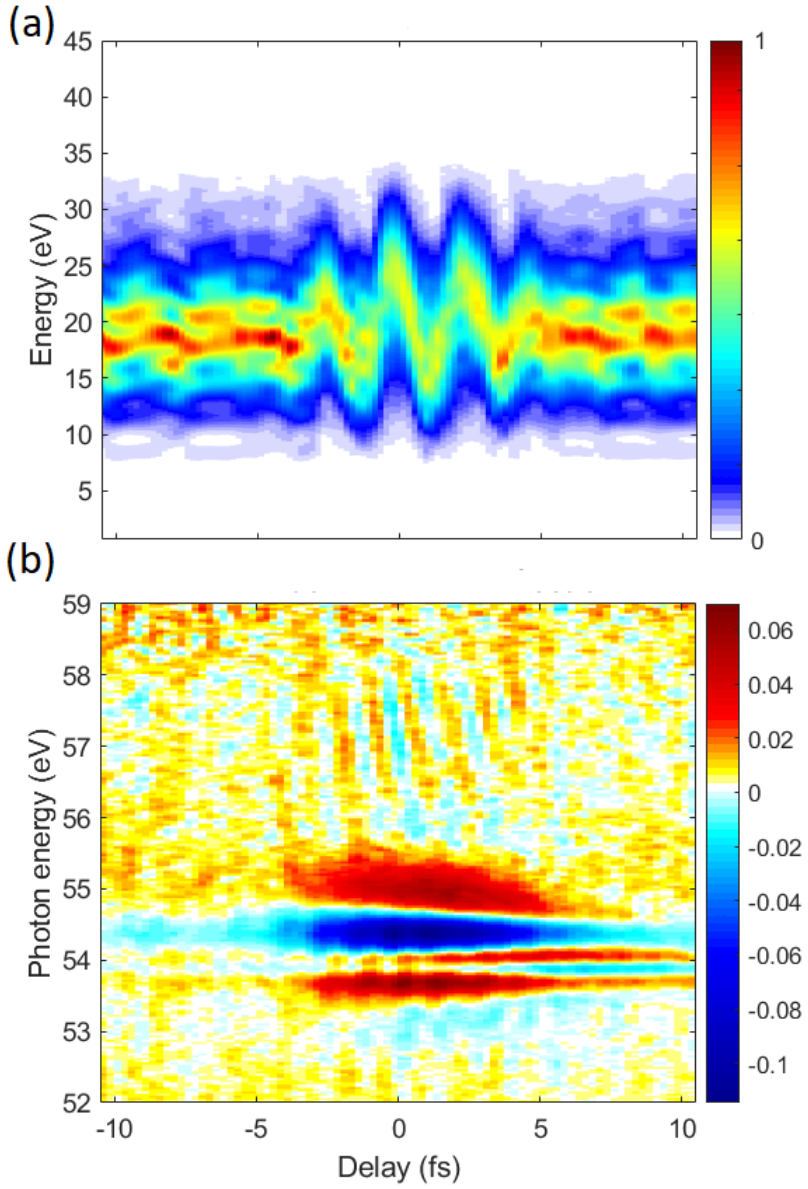

Figure 3.9: Experimental traces simultaneously acquired in the two foci of the attosecond transient reflectivity spectroscopy beamline. (a) Photoelectron streaking trace acquired in Ne gas in the first focus. (b) Transient reflection trace acquired on a (100) cut MgF_2 sample in the second focus.

pulse as the object to reconstruct, one can adapt this retrieval algorithm to the temporal domain, and use it to completely characterize both the NIR-VIS and the XUV pulses. In the present experimental condition, the single XUV attosecond pulse ionizes the neon gas atom target of the TOF spectrometer at different delays with respect to the center of the IR pulse. After ionization, the photoelectron wave packet in the continuum of states, feels the force exerted by the electric field of the infrared pulse, that will change its momentum. The photoelectron spectrum is then streaked by the presence of the NIR-VIS field (see Section 1.1.2). It is possible to prove [35, 87] that the center of mass of the photoelectron spectrum, defined as:

$$E_{CoM}(\tau) = \int_0^{+\infty} E\ S(E,\tau)dE \tag{3.40}$$

where $S(E,\tau)$ is the normalized photoelectron spectrum at a delay τ and E is the photoelectron energy, will follow the vector potential of the field $(-\mathbf{A}(t))$, allowing for its direct measurement. In order to get a streaking trace that could be well treated by ePIE algorithm, as it is presented in the left panel of Figure 3.9, we preformed a linear background subtraction and a smoothing using a moving mean filter in the direction of the energy axis. We then applied to this trace the ePIE retrieval algorithm (1000 iterations) twenty times, starting form slightly different initial conditions. The retrieved XUV and NIR-VIS pulses are reported in Figure 3.10. The extracted full-width at half-maximum duration of the near infrared pulse is equal to 4.7 $\pm$ 0.3 fs, and it is possible to notice the presence of a small pre-pulse and of a

small after-pulse. Concerning the XUV single attosecond pulse, the reconstructed full-width at half-maximum duration is 211 ± 3 as.

It can be useful, however, to quickly extract the information about the NIR-VIS field vector potential directly from the center of mass of the photoelectron trace (Figure 3.11).

3.5.2 Time Axis Calibration

We can use the information we gather from the streaking field to finely calibrate the delay axis. If we extract the envelope of the center of mass, for example, we can assume that it will be maximum when the reciprocal delay between the XUV single attosecond pulse and the IR pulse is zero. In order to set the 0 time delay of our experiment, then, we fitted the center of mass of our streaking trace with a Gaussian function, multiplied by a cosine function, on the experimental delay axis:

$$A + b\cos(2ft + c)e^{-((t-b1)/c1)^2}, \tag{3.41}$$

where A, b, c, f, $b1$ and $c1$ are free parameters. The result of the fit is shown in Figure 3.12. We then assume $b1$, which is the temporal position of the maximum of the Gaussian function, as the zero time delay.

In ATRS experiments, moreover, it can be useful to know exactly the phase difference between the NIR pump field and possible oscillations in the transient reflectivity trace, in order to

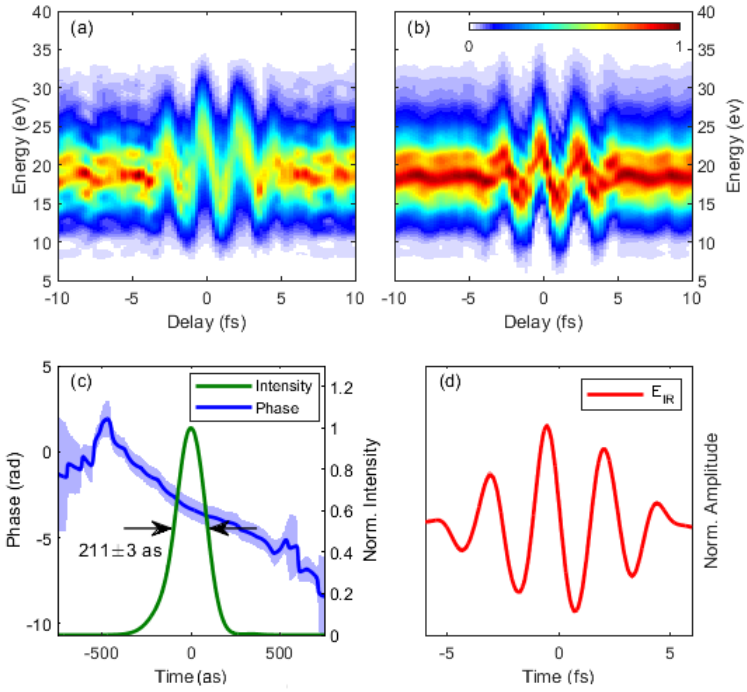

Figure 3.10: ePIE algorithm reconstruction of the experimental streaking trace acquired in neon. (a) Experimental trace. (b) Reconstructed trace. (c) Reconstructed temporal intensity profile and phase of the XUV pulse. (d) Reconstructed electric field of the IR pulse. Confidence intervals are calculated over 20 reconstructions with slightly different initial guesses.

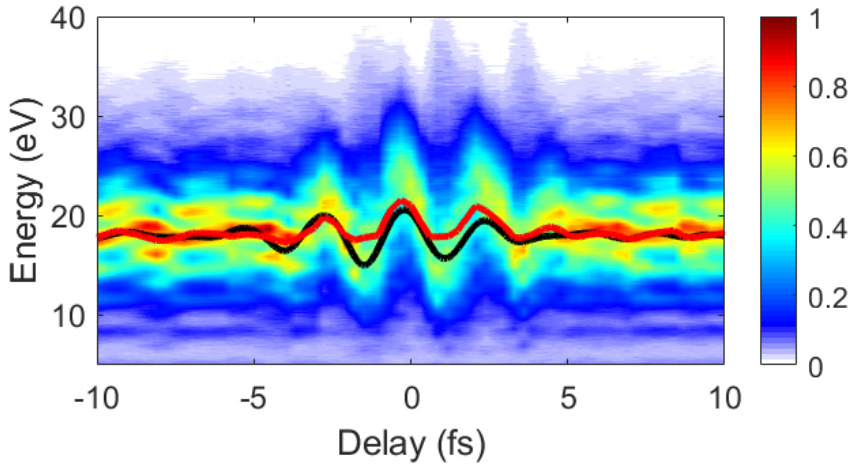

Figure 3.11: Comparison between the extracted center of mass of the streaking trace (red line) and the reconstructed vector potential (black line).

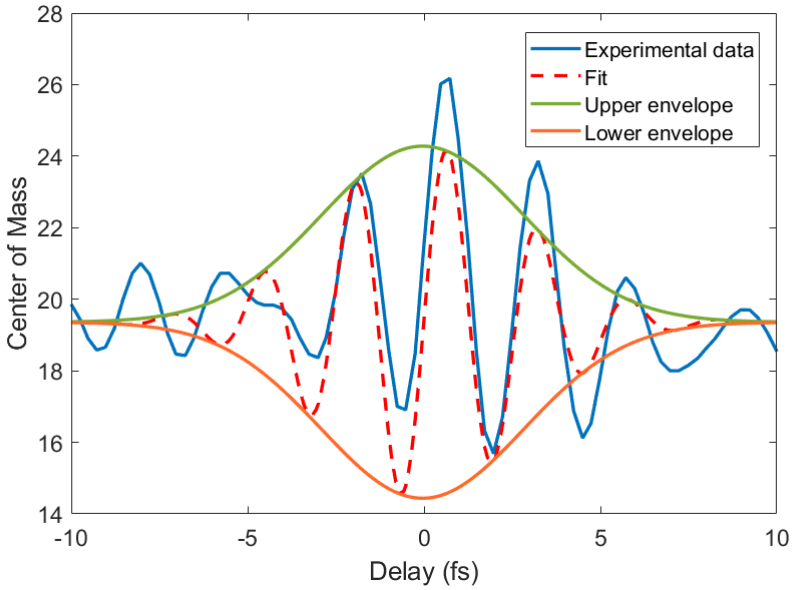

Figure 3.12: Blue solid line: center of mass extracted from the experimental photoelectron trace. Red dashed line: fitting of the experimental trace with the function $A+b\cos(2ft+c)e^{-((t-b1)/c1)^2}$. The temporal position of the maximum of the Gaussian function was assumed as the zero time delay. Green solid line and orange solid line: upper and lower envelope of the Gaussian fit, respectively.

distinguish different types of electron motion (e.g. intraband vs interband motion) as done in [18]. However, since the streaking measurement to retrieve the experimental NIR-VIS vector potential cannot be performed right on the solid sample site, we had to perform a reference experiment to measure the relative phase accumulated in the refocusing path. This experiment consists in the simultaneous acquisition of two RABBITT (see Section 1.1.1) traces acquired placing two TOF spectrometers in the two foci of the setup, where noble gas targets had been set. We want to investigate how the term θ_{NIR} in equation 1.3, changes because of the refocusing path. To do so, we used the same gas target in the two foci to assure that the atomic contribution is equivalent in the two interaction regions, $\Delta\theta_{2q}^{At,(1)} = \Delta\theta_{2q}^{At,(2)} = \Delta\theta_{2q}^{Ne}$. As demonstrated for an analog experiment in [88], moreover, the effect of the interaction in the first target and of the refocusing mirror on the phase of the XUV beam in the second target is negligible. Thus, the term $\Delta\theta_{HH}$ can be considered unchanged between the two targets. We can thus estimate the phase accumulated by the NIR pulse in the reflection on the toroidal refocusing mirror as:

$$\theta_{NIR}^{mirror} = \Theta_{2q}^{(1)} - \Theta_{2q}^{(2)}, \tag{3.42}$$

where $\Theta_{2q}^{(1)}$ and $\Theta_{2q}^{(2)}$ are the phase extracted from the oscillation of the SB with order $2q$ in the first and second TOF spectrometer, respectively.

The calibration measurement results are reported in Figures 3.13 and 3.14. In the upper panel of Figure 3.14, the measured

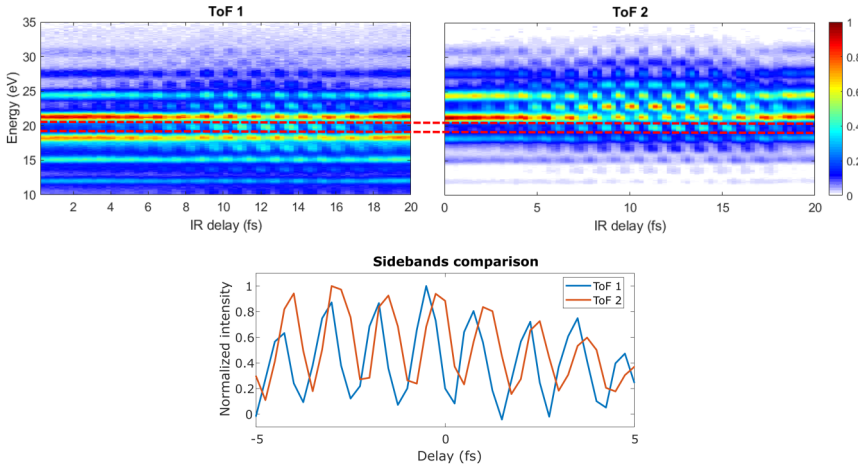

Figure 3.13: Upper panel: on the right, the photoelctron trace acquired in the first focus of the setup; on the left, the photoelctron trace acquired in the second focus of the setup. Lower panel: integrated signal of two corresponding sidebands identified by the red dashed lines in the upper panel, showing a slightly different phase.

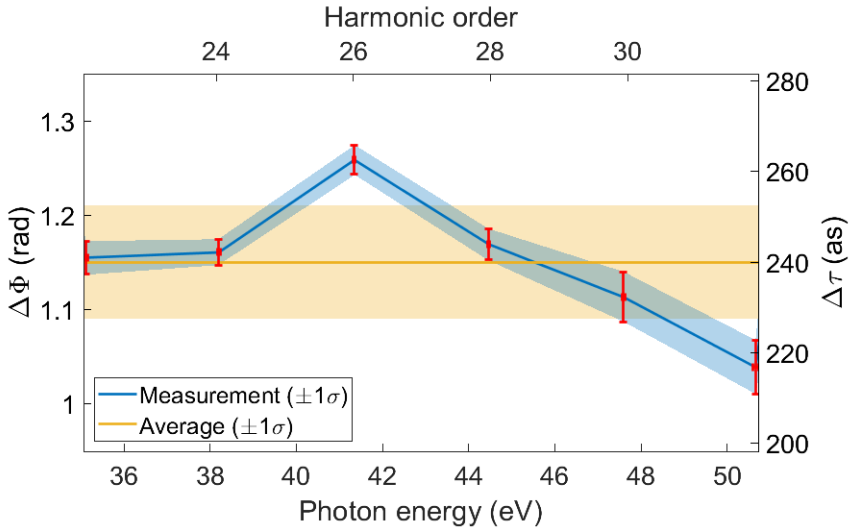

Figure 3.14: Phase difference (delay) accumulated in the refocusing path for different XUV photon energies (corresponding to different sidebands). The yellow line and shaded area represents the mean value.

accumulated NIR phase in the refocusing process is shown as a function of the XUV photon energy. It results to be almost flat over all the considered energy range. Therefore, the calibration of our delay axis in the experimental transient reflectivity trace was performed assuming a phase displacement equal to the mean value of the measured accumulated phase, which results to be (1.1472 ± 0.0566) rad, corresponding to about (238 ± 11.7) as.

3.5.3 ATRS Trace Analysis

The experimental relative variation of MgF_2 reflectivity in the XUV spectral region, as a function of the XUV-NIR delay and of the photon enerdy, is reported in Figure 3.15b. The experimental trace was acquired in the energy region of the excitonic features of MgF_2 reported in section 3.2. The system was perturbed by a NIR-VIS 6-fs pump pulse, giving a Keldysh parameter value of $\gamma \simeq 3.95$, inducing multiphoton absorption and intraband motion within the conduction band and the excitonic states. The dynamics around the excitonic region are then probed by detecting the relative variation in reflectivity of a broadband attosecond XUV probe pulse (see Figure 3.15a). The relative differential transient reflectivity is calculated as stated in Equation 3.39.

The very first observation that we can make is that there are two different kind of dynamics. Some few femtosecond dynamics are visible in the region of the excitonic features (around 54.6 eV), and faster oscillations at twice the pump frequency are present around the exciton and in the conduction band region (above

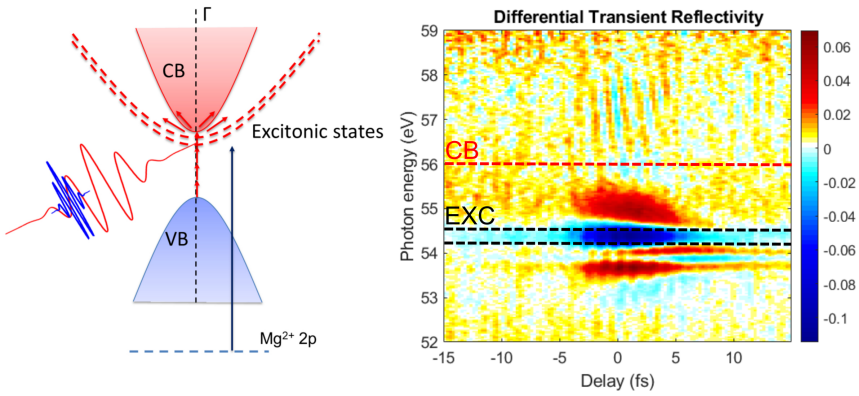

Figure 3.15: Left panel: Schematic representation of the pump-probe experiment on MgF_2. VB stands for Valence Band. CB stands for Conduction Band. Red arrows schematically represent the effects of NIR-VIS field on the sample (multiphoton absorption and intraband motion) around the Γ point. Blue arrow represents the XUV field probing around the exciton region. Right panel: Experimental ATRS trace on MgF_2. Red dashed line marks the position of the bottom of the conduction band with respect to Mg^{2+} 2p orbitals. Black dasked lines mark the position of the excitonic states with respect to Mg^{2+} 2p orbitals. Positive delays means NIR-VIS pulse comes first. Peak intensity of near-infrared pump pulse: $(1.32 \pm 0.07) \times 10^{13}$ W/cm^2. For any pump-probe delay step, 120 different spectra with and without the NIR-VIS pump pulse were averaged. Each spectrum was obtained with an exposure time of the CCD camera of the XUV spectrometer of 0.1 s.

$\sim$ 56 eV).

In the following, I will present the analysis we performed on the experimental results. In the first part, I will introduce the results we obtained by fitting the trace with an ad hoc more refined fitting model developed by us, starting from the fitting method reported by Moulet *et al.* in their ATAS study of core excitons dynamics in SiO_2 [17]. I will, then, report and discuss two possible theoretical model for the description of the experimental measurement developed in collaboration with the research group of Prof. A. Rubio (Max Planck Institute for the Structure and Dynamics of Matter - Hamburg).

Fitting Model

For a first quantitative analysis of the experimental trace, we tried to fit the ATRS trace using a theoretical model, presented in [89], used to give a physical description to absorption spectra. It consists in a simple classical model which, in particular, simulates the time-dependent response of the dipole moment produced by the XUV photons, in the presence of an IR pulse.

First of all, let's assume the exciton temporal evolution as an instantaneous population creation at the energy ω_e followed by an exponential population decay having a time constant T_e. We can write the exciton dipole moment $d(t)$, as:

$$d(t) \propto \theta(t) e^{-\frac{t}{2T_e}} e^{-i\omega_e t}, \tag{3.43}$$

where $\theta(t)$ is the Heaviside function. Then, we can take into account the many-body relaxation resulting from scattering of the exciton with phonons by defining another term:

$$\Phi(t) = \frac{M_0^2}{\omega_p^2}[(2N+1)(1-\cos\omega_p t - i(\omega_p t - \sin\omega_p t)], \quad (3.44)$$

where M_0 is the coupling strength of the phonons with the electric dipole, ω_p is the phonon energy and $N = e^{-\frac{\hbar\omega_p}{k_B T}}$ (being k_B the Boltzman constant and T the temperature) is the phonon population, we can write:

$$d(t) \propto \theta(t) e^{-\frac{t}{2T_e}} e^{-i\omega_e t} e^{-\Phi(t)}. \quad (3.45)$$

Finally, in order to consider the effect of the IR pulse in the pump-probe experiment, we can add a last additional term:

$$\Phi_L(t,\tau) = -\left(\gamma + i\frac{\alpha}{2}\right)\int_0^t E^2(t'-\tau)dt', \quad (3.46)$$

where τ is the delay between the XUV and IR pulses, γ accounts for amplitude reduction resulting from the IR field-induced coupling of the soft x-ray dipole with nearby electronic states and α is the polarizability. The dipole element,thus, becomes:

$$d(t) \propto \theta(t) e^{-\frac{t}{2T_e}} e^{-i\omega_e t} e^{\Phi(t)} e^{\Phi_L(t,\tau)}. \quad (3.47)$$

Then, we tried to recast the so-retrieved dielectric dipole in the time domain to the energy-dependent reflectivity signal we measure. Let N_p be the density of XUV-induced electric dipole.

The polarization can be written as $P(t,\tau) = N_p d(t,\tau)$. Transforming to the frequency domain, we obtain $P(\omega,\tau) = N_p d(\omega,\tau)$. Since $P(\omega,\tau) = \chi(\omega,\tau)E_{XUV}(\omega)$ (where $\chi(\omega,\tau)$ is the electrical susceptibility of the medium), we can obtain the electrical permittivity in the XUV spectral range as follows:

$$\epsilon(\omega,\tau) = 1 + \chi(\omega,\tau) = 1 + \frac{N_p}{E_{XUV}(\omega)} d(\omega,\tau) \tag{3.48}$$

To model this, we write $\epsilon(\omega,\tau)$ as:

$$\epsilon(\omega,\tau) = \epsilon_0 + k\mathcal{F}[\theta(t)e^{-\frac{t}{2T_e}} e^{-i\omega_e t} e^{\Phi(t)} e^{\Phi_L(t,\tau)}] \tag{3.49}$$

where ϵ_0 accounts for a baseline permittivity that may differ from 1, and k accounts for the dipole density (unknown) and XUV field spectrum. Notice that we assumed the XUV spectrum to be constant in the energy region under investigation. We can then relate the electrical permittivity to the reflectivity using the Fresnel equation (in our case, for s-polarization):

$$R_s(\omega,\tau) = \left| \frac{n_1 \cos\theta_i - \sqrt{\epsilon(\omega,\tau) - n_1 \sin^2\theta_i}}{n_1 \cos\theta_i + \sqrt{\epsilon(\omega,\tau) - n_1 \sin^2\theta_i}} \right| \tag{3.50}$$

Where n_1 is the refractive index of the medium and θ_i the angle of incidence. Since, in our case, we have two excitons involved in our experiment, as described in section 3.3.2, we modified the model to account for the second exciton as well. To do so, we

simply computed a weighted sum of the two reflectance values, as follow:

$$R_s(\omega,\tau) = aR_s^{(1)}(\omega,\tau) + (1-a)R_s^{(2)}(\omega,\tau) \qquad a \in [0,1]. \quad (3.51)$$

The relative variation of the reflectivity, is then computed, as a function of the XUV photon energy as follows:

$$\frac{\Delta R}{R} = \frac{R_s(\omega,\tau) - R_s(\omega,\tau_\infty)}{R_s(\omega,\tau_\infty)}, \quad (3.52)$$

where τ_∞ is a delay when the XUV and IR are not overlapped. This is the equation we need to fit the experimental data. In the model there are 17 free parameters:

- α_1, α_2, the polarizabilities
- γ_1, γ_2, the damping ratios
- M_{01}, M_{02}, the phonon couplings
- $\omega_{p,1}, \omega_{p,2}$, the phonon energies
- $\omega_{e,1}, \omega_{e,2}$, the exciton energies
- $T_{e,1}, T_{e,2}$, the decay time constants
- $\epsilon_{01}, \epsilon_{02}$, the baseline permittivities
- k_1, k_2, the permittivity factors
- a, the branching ratio.

To extract the values of these parameters from the model, we applied a non-linear least square data-fitting procedure, implementing a trust region reflective algorithm, trying to minimize the error function g(x), defined as follows:

$$g(x) = \left(\frac{\Delta R}{R}\right)^{th} - \left(\frac{\Delta R}{R}\right)^{ex} \tag{3.53}$$

where th stands for "theoretical model" and ex for "experimental".

As a first approach to the transient reflectivity trace, to be as accurate as possible, we considered, for the fit, the electric field extracted from the streaking trace. The fit result is shown in Figure 3.16a. It is possible to notice that the fit nicely reproduces the slower dynamics, while fails in correctly evaluate the 2ω-oscillations and in particular, the oscillations tilt. This probably happens because the model assumes constant material dielectric function over the whole energy range considered, thus totally neglecting all the possible dispersion. Therefore, being impossible to nicely reproduce the fast oscillations, we decided to use this model to fit only the slow components, after Fourier filtering of the experimental trace. To do so, we turned off the fast varying term in the model setting $\omega_{IR} = 0$. The results of the fit for the transient reflection trace are shown in Figure 3.16b. The model reproduces quite nicely all the dynamical features of the transient reflection trace. The numeric fit results are reported in Table 3.5.3. Interestingly, it was possible to extract values of the decay times for the excitonic features of $\tau_1 = 2T_1 = 2.09 \pm 0.003$fs and $\tau_2 = 2T_2 = 3.09 \pm 0.1$ fs (uncertainties are given by the con-

Parameter	Value
α_1	$2\pi(1.6570 \pm 0.09)$ eV Å^2 V^{-2} fs^{-1}
γ_1	$2\pi(1.2868 \pm 0.0087)$ eV Å^2 V^{-2} fs^{-1}
M_1	$2\pi(\sim 0)$ fs^{-1}
T_1	$(+1.0457 \pm 0.0014)$ fs
k_1	(-0.4035 ± 0.2)
$\omega_{p,1}$	(0.41 ± 0.05) rad fs^{-1}
$\omega_{e,1}$	(82.66 ± 0.03) rad fs-1
α_2	$2\pi(+1.64 \pm 0.1228)$ eV Å^2 V^{-2} fs^{-1}
γ_2	$2\pi(0.1137 \pm 0.0488)$ eV Å^2 V^{-2} fs^{-1}
M_2	$2\pi(0.3954 \pm 0.01)$ fs^{-1}
T_2	(1.5457 ± 0.04865) fs
k_2	(0.5644 ± 0.2)
$\omega_{p,1}$	(0.5141 ± 0.005) rad fs^{-1}
$\omega_{e,1}$	(81.82 ± 0.01) rad fs-1
a	0.7148

Table 3.1: Relevant fit parameters after optimization for transient reflection trace. The two baseline permittivities are just contant parameters needed for the correct static reflection fit.

fidence interval of the fit results). Moreover, it is worth noting that M_1 is very close to zero, meaning that the exciton-phonon coupling of the first exciton (the higher energy one) is very poor.

This simplified fitting model was, thus, able to give us interesting quantitative information about the observed transient reflectivity dynamics, expecially for the slow components. It was not possible, however, to fully reproduce the whole measured trace, since the description of fast oscillations requires a more refined model.

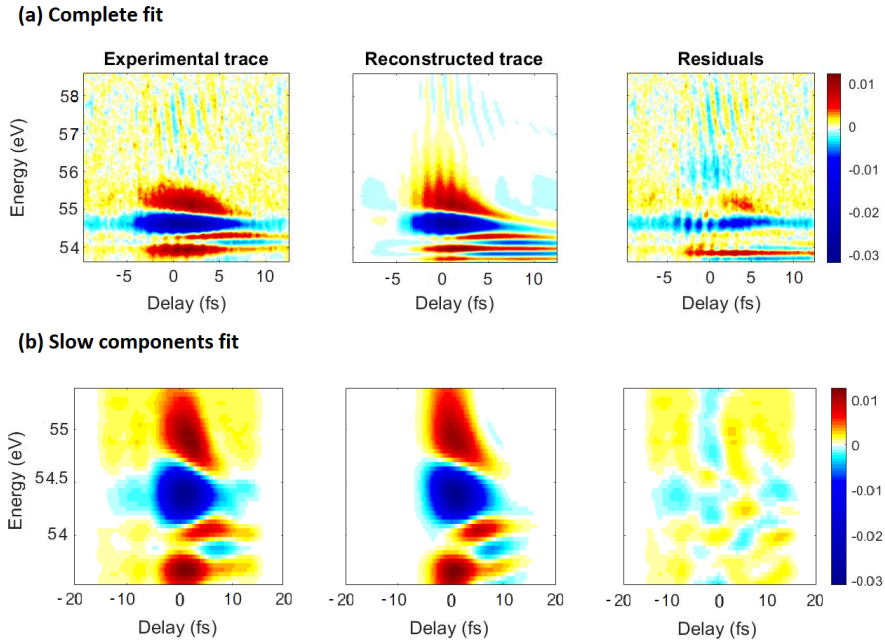

Figure 3.16: (a) Full simple model fitting and residuals. (b) Slow components simple model fitting and residuals. The extracted values of the decay times for the excitonic features are $\tau_1 = 2T_1 = 2.09 \pm 0.003$fs and $\tau_2 = 2T_2 = 3.09 \pm 0.1$ fs (uncertainties are given by the 95 % confidence interval of the fit results).

Theoretical Models

In order to exctract more information from the transient reflectivity trace, expecially about the oscillatory components, we established a collaboration with the research group of Prof. A. Rubio (Max Planck Institute for the Structure and Dynamics of Matter - Hamburg) to develop an ab initio more refined theoretical model for the description of the physical problem.

Two possible theoretical models to describe the processes under study are reported:

- A 3-level model for the exciton modeling
- A One-Dimensional Time-Dependent Hartree-Fock Model (1D-TDHF)

3-level Model. Each exciton peak dynamics of MgF_2 is modeled with a phenomenological three-level model. First, it is introduced a two-level model, such that the linear optical property of MgF_2 is reproduced, as reported in [1]. The total dielectric function is written as a sum of a base function and a dielectric response of 2-level system:

$$\epsilon^{TOT}(\omega) = \epsilon^{base}(\omega) + 4\pi\chi_{2-level}(\omega) \tag{3.54}$$

The 2-level system is described by the following Hamiltonian:

$$H(t) = \begin{pmatrix} \epsilon_c & E_{XUV}(t) \cdot d_{cs} \\ E_{XUV}(t) \cdot d_{cs} & \epsilon_s \end{pmatrix} \tag{3.55}$$

where, $E_{XUV}(t)$ is the XUV field, and ϵ_c and ϵ_s are respectively the energy states of the Mg $2p^{2+}$ semi-core level and of the s-state of the exciton. The dynamics of the two-level system is described by:

$$\frac{d\rho(t)}{dt} = \frac{[H(t), \rho(t)]}{i\hbar} - \frac{1}{T_2} \begin{pmatrix} 0 & \rho_{sc} \\ \rho_{cs} & 0 \end{pmatrix} \tag{3.56}$$

where $\rho(t)$ is the density matrix of the two-level system, and T_2 is the decoherence time, which defines the linewidth of the excitonic peak. The parameters, $\epsilon_s - \epsilon_c$, d_{cs}, and T_2 were chosen to ensure that the model reproduces the linear optical property of MgF_2. Then, a p-type excited state of the exciton was added to the system. The system Hamiltonian becomes:

$$H(t) = \begin{pmatrix} \epsilon_c & E_{XUV}(t) \cdot d_{cs} & 0 \\ E_{XUV}(t) \cdot d_{cs} & \epsilon_s & E_{IR}(t) \cdot d_{sp} \\ 0 & E_{IR}(t) \cdot d_{sp} & \epsilon_p \end{pmatrix} \tag{3.57}$$

where $E_{IR}(t)$ is the NIR field, coupling s and p exciton states. The energy difference between s and p states was set to 1.2 eV. This choice is based on the energy levels of the hydrogen atoms and may be refined. The same three level model was set for both the excitonic peaks (A and B) independently (see Figure 3.17 for a sketch of the states involved in this model). Pump-probe simulation were then performed for the two and summed with a proper factor ($\sim \frac{1}{3}$) to simulate the total pump-probe trace, that is shown in Figure 3.18. It is interesting to notice that, in

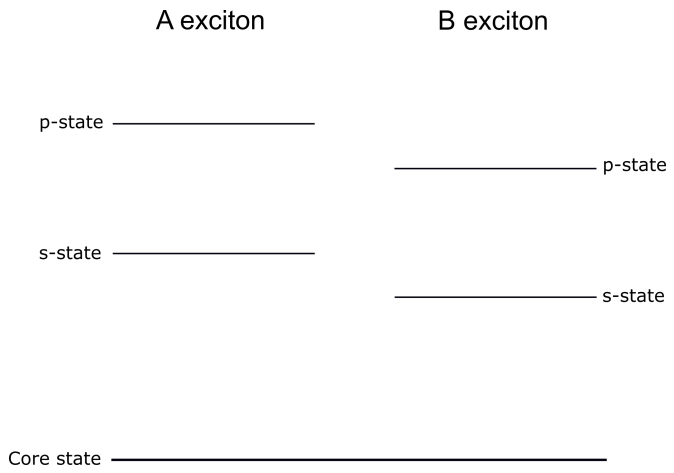

Figure 3.17: 3-level model energy level scheme. The core state of both A and B excitons is MgF_2 $2p^{2+}$.

this model, the presence of the MgF_2 crystal does not affect the Hamiltonian since no crystal potential is taken into account.

One-Dimensional Time-Dependent Hartree-Fock. Another possible approach is to develop a one-dimensional solid-state model based on the time-dependent Hartree-Fock (TDHF) method [90] to investigate the exciton dynamics. For this purpose, we consider the following Hamiltonian:

$$H = \sum_i \left[\frac{p_i^2}{2} + v_{ext}(x_i) \right] + \frac{1}{2} \sum_{i \neq j} w(x_i - x_j), \tag{3.58}$$

where v_{ext} is the external potential, given by a sum of the periodic lattice potential and a mean field attractive potential,

and $w(x)$ is the electron-electron interaction:

$$v_{ext}(x) = -V_0 \cos\left(\frac{2\pi x}{L}\right) - \sum_{n=-\infty}^{+\infty} \frac{4\alpha}{\sqrt{(x-nL)^2+1}}, \qquad (3.59)$$

and

$$w(x) = \frac{\alpha}{\sqrt{x^2+1}} \qquad (3.60)$$

Here, four electrons are considered in the single-cell, and the lattice constant L is set to 3.052 Å. We set V_0 to 0.125 a.u. and α to 0.88 a.u. so that the band gap of the system becomes 12.8 eV, as reported in [1], and the binding energy of the core-exciton becomes 1.2 eV. The transient optical-conductivity change was computed by theoretical pump-probe simulations. The pump pulse has a mean photon energy of 1.55 eV and a pulse width of 6 fs. The probe pulse has a mean photon energy of 45 eV and a pulse width of 250 as. The relative reflectance variation (shown in Figure 3.18) was then calculated starting from the optical absorption variation. Because of the difference of the dimension of the model and the real system, it is tricky to compare the results directly. On the other hand, the basic physics here is expected not to significantly depend on the dimension of the model. Since both the pump and the probe field are linearly polarized, the 1D model is expected to capture qualitatively the correct behavior of the system. Furthermore, the real MgF_2 reflectivity spectrum shows a double peak, due to the presence of two excitons (A and B). In order to compare the simulation result with the experiment,

we then have to model the dielectric function by the following formula:

$$\epsilon^{tot-model}(\omega) = \alpha + \\ + \left[\beta\epsilon^{1D-model}(\omega) + \frac{\beta}{3}\epsilon^{1D-model}(\omega+\Delta)\right], \quad (3.61)$$

where $\epsilon^{1D-model}$ is the dielectric function of the 1D model, α accounts for a baseline that may differ from 0 and is a complex parameter, β is a real parameter accounting for the different oscillator strength of the two excitons, and Δ is the spin-orbit split. The parameters, α and β, are chosen such that the static model dielectric function $\epsilon^{tot-model}$ shows the better agreement with the experimental static reflectivity. The same expression will be used for the transient reflectivity from the transient dielectric function of the 1D model.

Discussion. First of all, we checked if we could describe the system using the 3-level model (thus, completely discarding the presence of the crystal) or if the 1D-TDHF description (thus, the presence of the crystal) is strictly necessary to properly fit the data. To do so, we focused on the fast dynamics. We extracted the relative phase of the oscillations with respect to the VIS-NIR field vector potential (gathered from the data as described in Section 3.5.2), from the experimental trace as shown in the left panel of Figure 3.19. Then, we compared it with the one extracted from the theoretically computed trace for the 1D-TDHF

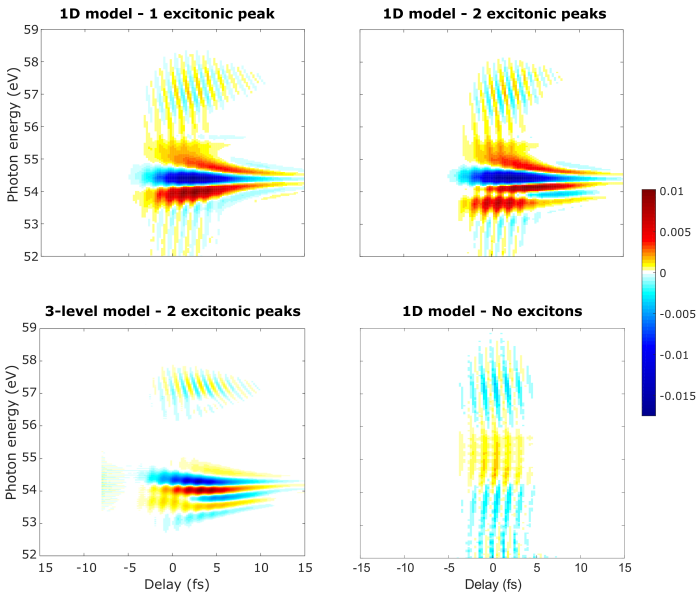

Figure 3.18: Simulated Attosecond Transient Reflectivity trace employing the different theoretical models described in the text. In the top left panel 1D Time Dependent Hartree Fock simulation is performed considering only the biggest excitonic peak. In the top right panel, the same simulation takes into account both the excitonic peaks as described by Equation 3.61. In the bottom left panel 3-level model simulation results are shown. Finally, in the bottom right panel, 1D-TDHF simulations considering only the crystal potential (no Coulombian exciton potential) are shown.

model, and the 3-level model. As it can be seen in the right panel of Figure 3.19, it looks like in the two different models, we have a different phase of the oscillations, and the one that best fits the experimental case is the 1D-TDHF one, suggesting that the presence of the crystal is fundamental for a proper description of the fast oscillations in the pump-probe trace. Further simulations, performed excluding the excitonic effects (see Figure 3.18), show that the interplay between the crystal and the core exciton strongly modifies the ultrafast response of the material, inducing an additional energy-dependent delay which amounts up to ~ 1 fs around the excitonic peak.

In conclusion, the possibility to perform ATRS experiments with the above described two-foci experimental setup, providing the possibility to fine tune the time delay axis knowing exactly the pump field acting on the sample, give us the possibility to gain an unprecedented insight into ultrafast dynamics is solids. In particular, with this experiment, we demonstrated the capability of our approach to measure electronic dynamics around a semi-core exciton with phase information that cannot be gathered in a different way.

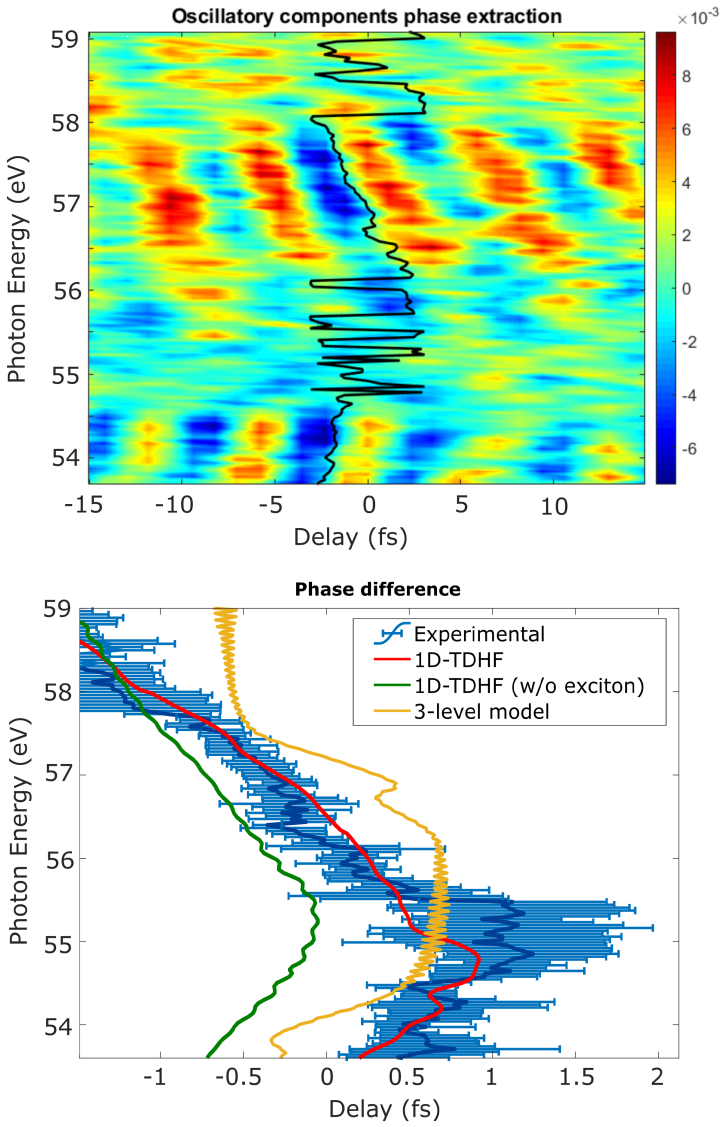

Figure 3.19: Top panel: relative phase of the oscillations with respect to the VIS-NIR field vector potential extracted from the experimental trace, after Fourier filtering of the slow-dynamic components. Bottom panel: comparison between the relative phase of the oscillations with respect to the VIS-NIR field vector potential extracted from the experimental trace, for the theoretically computed trace for the 3-level model, and for the one calculated with the 1D TDHF model with and without the inclusion of the excitons. The errorbar are given by the standard deviation calculated over 5 experimental transient reflectivity traces.

Chapter 4

Conclusions and Future Perspectives

This thesis reports important achievements in the study of attosecond electron dynamics in condensed matter. The novel two-foci NIR-XUV pump-probe beamline that we developed in the Attosecond Laboratories of Politecnico di Milano to perform Attosecond Transient Reflectivity Spectroscopy (ATRS) experiments is a very powerful tool for the investigation of ultrafast dynamics in solids with extreme temporal resolution, with the possibility to estimate with very high precision the NIR field acting on the sample.

The potential of the developed experimental setup is demonstrated with its application in the study of electron dynamics around a semi-core exciton in Magnesium Fluoride (MgF_2). We were able to measure the static reflectance of magnesium fluoride

in the XUV spectral region, and we confirmed the presence of two excitonic features already described in literature [1, 83]. We, then, used broadband XUV isolated attosecond pulses to probe the electron dynamics induced by high peak intensity NIR ~ 6 fs pump pulse around the excitonic peaks in an attosecond transient reflectifity spectroscopy fashion. Thanks to our sequential double-foci configuration, we were also able to finely calibrate the delay axis of the pump-probe measurement by acquiring a streaking trace in neon at the same time.

The acquired ATRS trace presents some slower (few femtoseconds) dynamics and some oscillations at twice the pump frequency with different phase for different photon energies. We quantitatively analyzed the few-femtosecond dynamics by means of a data fitting model developed from some simple physical considerations. Thus, we were able to extract decay times for the excitons of $\tau_1 = 0.8322 \pm 0.003$ fs and $\tau_2 = 1.3952 \pm 0.1$ fs. Moreover, in order to investigate the origin of the observed fast sub-cycle dynamics, we established a collaboration with the research group of Prof. A. Rubio (Max Planck Institute for the Structure and Dynamics of Matter - Hamburg) to develop a suitable theoretical model. As a preliminary result, two models have been developed, one considering each exciton as a 3-level system per se, and another one in which, taking into consideration a one dimensional crystal, a Time Dependent Hartree-Fock (1D TDHF) analysis has been performed. From an analysis of the oscillation phase, we could verify that the 1D TDHF best fits the experimental data, suggesting that the presence of the crystal is fundamental for a proper description of the fast oscillations in

the pump-probe trace. Further simulations, performed excluding the excitonic effects, showed that the interplay between the crystal and the core exciton strongly modifies the ultrafast response of the material, inducing an additional energy-dependent delay which amounts up to ~ 1 fs around the excitonic peak.

In conclusion, the work reported in this thesis offers unprecedented insights about core exciton dynamics in crystalline solids showing, at the same time, the potentials of our newly built two-foci beamline for attosecond transient reflectivity spectroscopy. In perspective, the application of this setup to the study of ultrafast electron dynamics in many different solid materials will be useful for a deeper understanding of light-matter interaction processes and strong field driven electron dynamics, to ultimately advance technological progress toward the development of PHz electronics and of ultrafast electronic switches.

Bibliography

[1] W. F. Hanson, E. T. Arakawa, and M. W. Williams. Optical properties of mgo and mgf2 in the extreme ultraviolet region. *Journal of Applied Physics*, 43(4):1661–1665, 1972.

[2] Wm. R. Lambert, P. M. Felker, and A. H. Zewail. Quantum beats and dephasing in isolated large molecules cooled by supersonic jet expansion and excited by picosecond pulses: Anthracene. *The Journal of Chemical Physics*, 75(12):5958–5960, 1981.

[3] R. L. Fork, C. H. Brito Cruz, P. C. Becker, and C. V. Shank. Compression of optical pulses to six femtoseconds by using cubic phase compensation. *Opt. Lett.*, 12(7):483–485, Jul 1987.

[4] Ahmed H. Zewail. Femtochemistry atomic scale dynamics of the chemical bond. *The Journal of Physical Chemistry A*, 104(24):5660–5694, 2000.

[5] K. Sokolowski-Tinten, C. Blome, C. Dietrich, A. Tarasevitch, M. Horn von Hoegen, D. von der Linde, A. Cavalleri,

J. Squier, and M. Kammler. Ultrafast structural dynamics in solids investigated with femtosecond x-ray pulses. *Applications of High Field and Short Wavelength Sources IX*, page TuD2, 2001.

[6] M. Lewenstein, Ph. Balcou, M. Yu. Ivanov, Anne L'Huillier, and P. B. Corkum. Theory of high-harmonic generation by low-frequency laser fields. *Phys. Rev. A*, 49:2117–2132, Mar 1994.

[7] Jeffrey L. Krause, Kenneth J. Schafer, and Kenneth C. Kulander. High-order harmonic generation from atoms and ions in the high intensity regime. *Phys. Rev. Lett.*, 68:3535–3538, Jun 1992.

[8] K. J. Schafer, Baorui Yang, L. F. DiMauro, and K. C. Kulander. Above threshold ionization beyond the high harmonic cutoff. *Phys. Rev. Lett.*, 70:1599–1602, Mar 1993.

[9] P. B. Corkum. Plasma perspective on strong field multiphoton ionization. *Phys. Rev. Lett.*, 71:1994–1997, Sep 1993.

[10] P. M. Paul, E. S. Toma, P. Breger, G. Mullot, F. Augé, Ph. Balcou, H. G. Muller, and P. Agostini. Observation of a train of attosecond pulses from high harmonic generation. *Science*, 292(5522):1689–1692, 2001.

[11] M. Hentschel, R. Kienberger, Ch Spielmann, G. A. Reider, N. Milosevic, T. Brabec, P. Corkum, U. Heinzmann, M. Drescher, and F. Krausz. Attosecond metrology. *Nature*, 414:509 EP –, Nov 2001. Article.

[12] Antti-Pekka Jauho and Kristinn Johnsen. Dynamical franz-keldysh effect. *Physical Review Letters*, 76, 12 1995.

[13] A. L. Cavalieri, N. Müller, Th Uphues, V. S. Yakovlev, A. Baltuska, B. Horvath, B. Schmidt, L. Blümel, R. Holzwarth, S. Hendel, M. Drescher, U. Kleineberg, P. M. Echenique, R. Kienberger, F. Krausz, and U. Heinzmann. Attosecond spectroscopy in condensed matter. *Nature*, 449(7165):1029–1032, 2007.

[14] Renate Pazourek, Stefan Nagele, and Joachim Burgdörfer. Attosecond chronoscopy of photoemission. *Rev. Mod. Phys.*, 87:765–802, Aug 2015.

[15] M. Lucchini, S. A. Sato, A. Ludwig, J. Herrmann, M. Volkov, L. Kasmi, Y. Shinohara, K. Yabana, L. Gallmann, and U. Keller. Attosecond dynamical franz-keldysh effect in polycrystalline diamond. *Science*, 353(6302):916–919, 2016.

[16] Hiroki Mashiko, Katsuya Oguri, Tomohiko Yamaguchi, Akira Suda, and Hideki Gotoh. Petahertz optical drive with wide-bandgap semiconductor. *Nature Physics*, 12:741 EP –, Apr 2016.

[17] A. Moulet, J. B. Bertrand, T. Klostermann, A. Guggenmos, N. Karpowicz, and E. Goulielmakis. Soft x-ray excitonics. *Science*, 357(6356):1134–1138, 2017.

[18] F. Schlaepfer, M. Lucchini, S. A. Sato, M. Volkov, L. Kasmi, N. Hartmann, A. Rubio, L. Gallmann, and U. Keller. At-

tosecond optical-field-enhanced carrier injection into the gaas conduction band. *Nature Physics*, 14(6):560–564, 2018.

[19] Michael Zürch, Hung-Tzu Chang, Lauren J. Borja, Peter M. Kraus, Scott K. Cushing, Andrey Gandman, Christopher J. Kaplan, Myoung Hwan Oh, James S. Prell, David Prendergast, Chaitanya D. Pemmaraju, Daniel M. Neumark, and Stephen R. Leone. Direct and simultaneous observation of ultrafast electron and hole dynamics in germanium. *Nature Communications*, 8(1):15734, 2017.

[20] Christopher J. Kaplan, Peter M. Kraus, Andrew D. Ross, Michael Zürch, Scott K. Cushing, Marieke F. Jager, Hung-Tzu Chang, Eric M. Gullikson, Daniel M. Neumark, and Stephen R. Leone. Femtosecond tracking of carrier relaxation in germanium with extreme ultraviolet transient reflectivity. *Phys. Rev. B*, 97:205202, May 2018.

[21] Francesca Calegari, Giuseppe Sansone, Salvatore Stagira, Caterina Vozzi, and Mauro Nisoli. Advances in attosecond science. *Journal of Physics B: Atomic, Molecular and Optical Physics*, 49(6):062001, feb 2016.

[22] M. Schultze, M. Fieß, N. Karpowicz, J. Gagnon, M. Korbman, M. Hofstetter, S. Neppl, A. L. Cavalieri, Y. Komninos, Th. Mercouris, C. A. Nicolaides, R. Pazourek, S. Nagele, J. Feist, J. Burgdörfer, A. M. Azzeer, R. Ernstorfer, R. Kienberger, U. Kleineberg, E. Goulielmakis, F. Krausz, and V. S. Yakovlev. Delay in photoemission. *Science*, 328(5986):1658–1662, 2010.

[23] K. Klünder, J. M. Dahlström, M. Gisselbrecht, T. Fordell, M. Swoboda, D. Guénot, P. Johnsson, J. Caillat, J. Mauritsson, A. Maquet, R. Taïeb, and A. L'Huillier. Probing single-photon ionization on the attosecond time scale. *Phys. Rev. Lett.*, 106:143002, Apr 2011.

[24] J.M. Dahlström, D. Guénot, K. Klünder, M. Gisselbrecht, J. Mauritsson, A. L'Huillier, A. Maquet, and R. Taïeb. Theory of attosecond delays in laser-assisted photoionization. *Chemical Physics*, 414:53 – 64, 2013. Attosecond spectroscopy.

[25] Mauro Nisoli, Piero Decleva, Francesca Calegari, Alicia Palacios, and Fernando Martín. Attosecond electron dynamics in molecules. *Chemical Reviews*, 117(16):10760–10825, Aug 2017.

[26] S. Neppl, R. Ernstorfer, A. L. Cavalieri, C. Lemell, G. Wachter, E. Magerl, E. M. Bothschafter, M. Jobst, M. Hofstetter, U. Kleineberg, J. V. Barth, D. Menzel, J. Burgdörfer, P. Feulner, F. Krausz, and R. Kienberger. Direct observation of electron propagation and dielectric screening on the atomic length scale. *Nature*, 517(7534):342–346, 2015.

[27] Fabian Siek, Sergej Neb, Peter Bartz, Matthias Hensen, Christian Strüber, Sebastian Fiechter, Miquel Torrent-Sucarrat, Vyacheslav M. Silkin, Eugene E. Krasovskii, Nikolay M. Kabachnik, Stephan Fritzsche, Ricardo Díez Muiño, Pedro M. Echenique, Andrey K. Kazansky, Norbert Müller,

Walter Pfeiffer, and Ulrich Heinzmann. Angular momentum–induced delays in solid-state photoemission enhanced by intra-atomic interactions. *Science*, 357(6357):1274–1277, 2017.

[28] M. Ossiander, J. Riemensberger, S. Neppl, M. Mittermair, M. Schäffer, A. Duensing, M. S. Wagner, R. Heider, M. Wurzer, M. Gerl, M. Schnitzenbaumer, J. V. Barth, F. Libisch, C. Lemell, J. Burgdörfer, P. Feulner, and R. Kienberger. Absolute timing of the photoelectric effect. *Nature*, 561(7723):374–377, 2018.

[29] L. Seiffert, Q. Liu, S. Zherebtsov, A. Trabattoni, P. Rupp, M. C. Castrovilli, M. Galli, F. Süßmann, K. Wintersperger, J. Stierle, G. Sansone, L. Poletto, F. Frassetto, I. Halfpap, V. Mondes, C. Graf, E. Rühl, F. Krausz, M. Nisoli, T. Fennel, F. Calegari, and M. ?. F. Kling. Attosecond chronoscopy of electron scattering in dielectric nanoparticles. *Nature Physics*, 13(8):766–770, 2017.

[30] H.G. Muller, P. Agostini, and Ph. Balcou. *Characterization of attosecond pulse trains from high-harmonic generation*, pages 209–218.

[31] P. M. Paul, E. S. Toma, P. Breger, G. Mullot, F. Augé, Ph. Balcou, H. G. Muller, and P. Agostini. Observation of a train of attosecond pulses from high harmonic generation. *Science*, 292(5522):1689–1692, 2001.

[32] P. M. Paul, E. S. Toma, P. Breger, G. Mullot, F. Augé, Ph.

Balcou, H. G. Muller, and P. Agostini. Observation of a train of attosecond pulses from high harmonic generation. *Science*, 292(5522):1689–1692, 2001.

[33] Eugene P. Wigner. Lower limit for the energy derivative of the scattering phase shift. *Phys. Rev.*, 98:145–147, Apr 1955.

[34] Reto Locher, Luca Castiglioni, Matteo Lucchini, Michael Greif, Lukas Gallmann, Jürg Osterwalder, Matthias Hengsberger, and Ursula Keller. Energy-dependent photoemission delays from noble metal surfaces by attosecond interferometry. *Optica*, 2(5):405–410, May 2015.

[35] J. Itatani, F. Quéré, G. L. Yudin, M. Yu. Ivanov, F. Krausz, and P. B. Corkum. Attosecond streak camera. *Phys. Rev. Lett.*, 88:173903, Apr 2002.

[36] Y. Mairesse and F. Quéré. Frequency-resolved optical gating for complete reconstruction of attosecond bursts. *Phys. Rev. A*, 71:011401, Jan 2005.

[37] Rick Trebino and Daniel J. Kane. Using phase retrieval to measure the intensity and phase of ultrashort pulses: frequency-resolved optical gating. *J. Opt. Soc. Am. A*, 10(5):1101–1111, May 1993.

[38] Daniel J. Kane. Real-time measurement of ultrashort laser pulses using principal component generalized projections. *J. Select Topics Quantum Electron*, 4(2), March 1998.

[39] J. Gagnon, E. Goulielmakis, and V.S. Yakovlev. The accurate frog characterization of attosecond pulses from streaking measurements. *Applied Physics B*, 92(1):25–32, Jul 2008.

[40] P. D. Keathley, S. Bhardwaj, J. Moses, G. Laurent, and F. X. Kärtner. Volkov transform generalized projection algorithm for attosecond pulse characterization. 18(7):14, 2016.

[41] Andrew M. Maiden and John M. Rodenburg. An improved ptychographical phase retrieval algorithm for diffractive imaging. *Ultramicroscopy*, 109(10):1256 – 1262, 2009.

[42] M. Ossiander, F. Siegrist, V. Shirvanyan, R. Pazourek, A. Sommer, T. Latka, A. Guggenmos, S. Nagele, J. Feist, J. Burgdörfer, R. Kienberger, and M. Schultze. Attosecond correlation dynamics. *Nature Physics*, 13(3):280–285, 2017.

[43] A. L. Cavalieri, N. Müller, Th Uphues, V. S. Yakovlev, A. Baltuska, B. Horvath, B. Schmidt, L. Blümel, R. Holzwarth, S. Hendel, M. Drescher, U. Kleineberg, P. M. Echenique, R. Kienberger, F. Krausz, and U. Heinzmann. Attosecond spectroscopy in condensed matter. *Nature*, 449(7165):1029–1032, 2007.

[44] W T Pollard and R A Mathies. Analysis of femtosecond dynamic absorption spectra of nonstationary states. *Annual Review of Physical Chemistry*, 43(1):497–523, 1992. PMID: 1463575.

[45] Lung Shan Kau, Darlene J. Spira-Solomon, James E. Penner-Hahn, Keith O. Hodgson, and Edward I. Solomon.

X-ray absorption edge determination of the oxidation state and coordination number of copper. application to the type 3 site in rhus vernicifera laccase and its reaction with oxygen. *Journal of the American Chemical Society*, 109(21):6433–6442, 1987.

[46] Tami E. Westre, Pierre Kennepohl, Jane G. DeWitt, Britt Hedman, Keith O. Hodgson, and Edward I. Solomon. A multiplet analysis of fe k-edge 1s $\rightarrow$ 3d pre-edge features of iron complexes. *Journal of the American Chemical Society*, 119(27):6297–6314, 1997.

[47] Eleftherios Goulielmakis, Zhi-Heng Loh, Adrian Wirth, Robin Santra, Nina Rohringer, Vladislav S. Yakovlev, Sergey Zherebtsov, Thomas Pfeifer, Abdallah M. Azzeer, Matthias F. Kling, Stephen R. Leone, and Ferenc Krausz. Real-time observation of valence electron motion. *Nature*, 466(7307):739–743, 2010.

[48] M. Holler, F. Schapper, L. Gallmann, and U. Keller. Attosecond electron wave-packet interference observed by transient absorption. *Phys. Rev. Lett.*, 106:123601, Mar 2011.

[49] P. Drude. Zur elektronentheorie der metalle; ii. teil. galvanomagnetische und thermomagnetische effecte. *Annalen der Physik*, 308(11):369–402, 1900.

[50] A. Sommerfeld and H. Bethe. *Elektronentheorie der Metalle*, pages 333–622. Springer Berlin Heidelberg, Berlin, Heidelberg, 1933.

[51] Felix Bloch. Über die quantenmechanik der elektronen in kristallgittern. *Zeitschrift für Physik*, 52(7):555–600, Jul 1929.

[52] Charles Kittel and Ching-Yao Fong. *Quantum theory of solids*. Wiley, 2010.

[53] Clarence Zener and Ralph Howard Fowler. A theory of the electrical breakdown of solid dielectrics. *Proceedings of the Royal Society of London. Series A, Containing Papers of a Mathematical and Physical Character*, 145(855):523–529, 1934.

[54] E.O. Kane. Zener tunneling in semiconductors. *Journal of Physics and Chemistry of Solids*, 12(2):181 – 188, 1960.

[55] *Elements of Solid State Theory*. Springer Berlin Heidelberg, Berlin, Heidelberg, 2007.

[56] David Emin and C. F. Hart. Existence of wannier-stark localization. *Phys. Rev. B*, 36:7353–7359, Nov 1987.

[57] Martin Schultze, Elisabeth M. Bothschafter, Annkatrin Sommer, Simon Holzner, Wolfgang Schweinberger, Markus Fiess, Michael Hofstetter, Reinhard Kienberger, Vadym Apalkov, Vladislav S. Yakovlev, Mark I. Stockman, and Ferenc Krausz. Controlling dielectrics with the electric field of light. *Nature*, 493(7430):75–78, 2013.

[58] L. V. Keldysh. Ionization in the field of a strong electromagnetic wave. 1964.

[59] Martin Schultze, Krupa Ramasesha, C.D. Pemmaraju, S.A. Sato, D. Whitmore, A. Gandman, James S. Prell, L. J. Borja, D. Prendergast, K. Yabana, Daniel M. Neumark, and Stephen R. Leone. Attosecond band-gap dynamics in silicon. *Science*, 346(6215):1348–1352, 2014.

[60] Romain Geneaux, Hugo J. B. Marroux, Alexander Guggenmos, Daniel M. Neumark, and Stephen R. Leone. Transient absorption spectroscopy using high harmonic generation: a review of ultrafast x-ray dynamics in molecules and solids. *Philosophical Tr ansactions of the Royal Society A: Mathematical, Physical and Engineering Sciences*, 377(2145):20170463, 2019.

[61] Ilana J. Porter, Scott K. Cushing, Lucas M. Carneiro, Angela Lee, Justin C. Ondry, Jakob C. Dahl, Hung-Tzu Chang, A. Paul Alivisatos, and Stephen R. Leone. Photoexcited small polaron formation in goethite (α-feooh) nanorods probed by transient extreme ultraviolet spectroscopy. *The Journal of Physical Chemistry Letters*, 9(14):4120–4124, 2018. PMID: 29985006.

[62] R. Locher, M. Lucchini, J. Herrmann, M. Sabbar, M. Weger, A. Ludwig, L. Castiglioni, M. Greif, M. Hengsberger, L. Gallmann, and U. Keller. Versatile attosecond beamline in a two-foci configuration for simultaneous time-resolved measurements. *Review of Scientific Instruments*, 85(1):013113, 2014.

[63] I. J. Sola, E. Mével, L. Elouga, E. Constant, V. Strelkov,

L. Poletto, P. Villoresi, E. Benedetti, J.-P. Caumes, S. Stagira, C. Vozzi, G. Sansone, and M. Nisoli. Controlling attosecond electron dynamics by phase-stabilized polarization gating. *Nature Physics*, 2(5):319–322, 2006.

[64] K. S. Budil, P. Salières, Anne L'Huillier, T. Ditmire, and M. D. Perry. Influence of ellipticity on harmonic generation. *Phys. Rev. A*, 48:R3437–R3440, Nov 1993.

[65] F. Ferrari, F. Calegari, M. Lucchini, C. Vozzi, S. Stagira, G. Sansone, and M. Nisoli. High-energy isolated attosecond pulses generated by above-saturation few-cycle fields. *Nature Photonics*, 4(12):875–879, 2010.

[66] Hiroki Mashiko, M. Justine Bell, Annelise R. Beck, Mark J. Abel, Philip M. Nagel, Colby P. Steiner, Joseph Robinson, Daniel M. Neumark, and Stephen R. Leone. Tunable frequency-controlled isolated attosecond pulses characterized by either 750 nm or 400 nm wavelength streak fields. *Opt. Express*, 18(25):25887–25895, Dec 2010.

[67] Hiroki Mashiko, Steve Gilbertson, Chengquan Li, Sabih D. Khan, Mahendra M. Shakya, Eric Moon, and Zenghu Chang. Double optical gating of high-order harmonic generation with carrier-envelope phase stabilized lasers. *Phys. Rev. Lett.*, 100:103906, Mar 2008.

[68] David J. Jones, Scott A. Diddams, Jinendra K. Ranka, Andrew Stentz, Robert S. Windeler, John L. Hall, and

Steven T. Cundiff. Carrier-envelope phase control of femtosecond mode-locked lasers and direct optical frequency synthesis. *Science*, 288(5466):635–639, 2000.

[69] C. Feng, J.-F. Hergott, P.-M. Paul, X. Chen, O. Tcherbakoff, M. Comte, O. Gobert, M. Reduzzi, F. Calegari, C. Manzoni, M. Nisoli, and G. Sansone. Complete analog control of the carrier-envelope-phase of a high-power laser amplifier. *Opt. Express*, 21(21):25248–25256, Oct 2013.

[70] H.R. Telle, G. Steinmeyer, A.E. Dunlop, J. Stenger, D.H. Sutter, and U. Keller. Carrier-envelope offset phase control: A novel concept for absolute optical frequency measurement and ultrashort pulse generation. *Applied Physics B*, 69(4):327–332, Oct 1999.

[71] M. Nisoli, S. De Silvestri, and O. Svelto. Generation of high energy 10 fs pulses by a new pulse compression technique. *Applied Physics Letters*, 68(20):2793–2795, 1996.

[72] L. P. Maguire, S. Szilagyi, and R. E. Scholten. High performance laser shutter using a hard disk drive voice-coil actuator. *Review of Scientific Instruments*, 75(9):3077–3079, 2004.

[73] M. Huppert, I. Jordan, and H. J. Wörner. Attosecond beamline with actively stabilized and spatially separated beam paths. *Review of Scientific Instruments*, 86(12):123106, 2015.

[74] M. Hentschel, R. Kienberger, Ch Spielmann, G. A. Reider, N. Milosevic, T. Brabec, P. Corkum, U. Heinzmann, M. Drescher, and F. Krausz. Attosecond metrology. *Nature*, 414(6863):509–513, 2001.

[75] H Ibach. *Solid-state physics : an introduction to principles of materials science*. Springer, Berlin New York, 2009.

[76] Jacov Frenkel. On the transformation of light into heat in solids. ii. *Physical Review*, 37(10):1276, 1931.

[77] R. S. Knox. *Collective Excitations in Solids*. Springer US, Boston, MA, 1983.

[78] Harold P. Hjalmarson, Helmut Büttner, and John D. Dow. Theory of core excitons. *Phys. Rev. B*, 24:6010–6019, Nov 1981.

[79] R. D. Carson and S. E. Schnatterly. X-ray emission from core excitons. *Phys. Rev. Lett.*, 59:319–322, Jul 1987.

[80] R. Buczko, G. Duscher, S. J. Pennycook, and S. T. Pantelides. Excitonic effects in core-excitation spectra of semiconductors. *Phys. Rev. Lett.*, 85:2168–2171, Sep 2000.

[81] Jouanin, C., Albert, J.P., and Gout, C. Band structure and optical properties of magnesium fluoride. *J. Phys. France*, 37(5):595–602, 1976.

[82] Marisa Scrocco. Electron-energy-loss and x-ray photoelectron spectra of mgf_2. *Phys. Rev. B*, 33:7228–7231, May 1986.

[83] P. Rabe, B. Sonntag, T. Sagawa, and R. Haensel. The optical absorption of mgf2, mgcl2, and mgbr2 in the vicinity of the mg l-shell transitions. *physica status solidi (b)*, 50(2):559–569, 1972.

[84] Jon Olav Grepstad and Johannes Skaar. Total internal reflection and evanescent gain. *Optics express*, 19(22):21404–21418, 2011.

[85] Andrew M. Maiden and John M. Rodenburg. An improved ptychographical phase retrieval algorithm for diffractive imaging. *Ultramicroscopy*, 109(10):1256 – 1262, 2009.

[86] M. Lucchini, M.H. Brügmann, A. Ludwig, L. Gallmann, U. Keller, and T. Feurer. Ptychographic reconstruction of attosecond pulses. *Opt. Express*, 23(23):29502–29513, Nov 2015.

[87] F. Quéré, J. Itatani, G. L. Yudin, and P. B. Corkum. Attosecond spectral shearing interferometry. *Phys. Rev. Lett.*, 90:073902, Feb 2003.

[88] F. Schlaepfer, A. Ludwig, M. Lucchini, L. Kasmi, M. Volkov, L. Gallmann, and U. Keller. Gouy phase shift for annular beam profiles in attosecond experiments. *Opt. Express*, 25(4):3646–3655, Feb 2017.

[89] G. D. Mahan. Emission spectra and phonon relaxation. *Phys. Rev. B*, 15:4587–4595, May 1977.

[90] M.H. Beck, A. Jäckle, G.A. Worth, and H.-D. Meyer. The multiconfiguration time-dependent hartree (mctdh) method: a highly efficient algorithm for propagating wavepackets. *Physics Reports*, 324(1):1 – 105, 2000.